Modeling, Design, and Optimization of a High-Speed Flywheel for an Energy Storage System

A Thesis

Presented in Partial Fulfillment of the Requirements for the

Degree of Master of Science

with a

Major in Mechanical Engineering

in the

College of Graduate Studies

by

Brenden F. Kaschmitter

Major Professor: Matthew Riley, Ph.D.

Committee Members: Michael Santora, Ph.D.; Edwin Odom, Ph.D.

Department Administrator: Steven Beyerlein, Ph.D.

April 2016

Authorization to Submit Thesis

This thesis of Brenden F. Kaschmitter, submitted for the degree of Master of Science with a Major in Mechanical Engineering and titled "Modeling, Design, and Optimization of a Flywheel for a Flywheel Energy Storage System," has been reviewed in final form. Permission, as indicated by the signatures and dates given below, is now granted to submit final copies to the College of Graduate Studies for Approval.

Major Professor: _____ Date: _____
Matthew Riley, Ph.D.

Committee Members: _____ Date: _____
Michael Santora, Ph.D.

_____ Date: _____
Edwin Odom, Ph.D.

Department Administrator: _____ Date: _____
Steven Beyerlein, Ph.D.

Abstract

Flywheel Energy Storage System (FESS) operating at high angular velocities have the potential to be an energy dense, long life storage device. Effective energy dense storage will be required for the colonization in extraterrestrial applications with intermittent power sources. High-speed FESS may outperform batteries in efficiency, charge cycle life, and energy density. To operate at high angular velocities, high-strength, light weight composites will be needed for structural integrity. This thesis describes modeling and design of a high-speed hubless rotor utilizing wrapped, continuous fiber composites. The materials needed for motor/generator operations will be included in this design. With the use of a heuristic optimization method, the maximum design and angular velocity will be found such that structural integrity will be maintained.

Acknowledgments

I would like to sincerely thank my professors, colleagues, family, and friends for their guidance and support throughout this project. I am especially grateful for the support and guidance provided my major professor, Dr. Matthew Riley. Without his support, I would not have continued on with my graduate degree. I would also like to thank my committee members, Dr. Michael Santora and Dr. Edwin Odom, for taking time out of their busy schedules to read this thesis and listen to my defense.

Without the support of the other members, this project would not be possible. I would like to extend my gratitude to the other members of this project:

Dr. Michael Santora,

Dr. Herbert Hess,

Dr. Joe Law,

Dr. Christine Berven,

Justin Pettingill.

Table of Contents

List of Figures

List of Tables

List of Abbreviations

AMB	Active Magnetic Bearing
FEA	Finite Element Analysis
FESS	Flywheel Energy Storage System
FRRM	Field Regulated Reluctance Machine
LHS	Latin Hypercube Sampling
NASA	National Aeronautics and Space Administration
PMB	Passive Magnetic Bearing
PSO	Particle Swarm Optimization
RVE	Representative Volume Element
UIFESS	University of Idaho Flywheel Energy Storage System
UPS	Uninterruptible Power Supply

Chapter 1. Introduction

1.1 Motivation

Whether it's production or storage, energy has been an important topic over the last several years. Nearly every aspect of modern civilization revolves around the use of energy. Energy becomes even more important when one is striving to establish and maintain a civilization on a lunar surface where natural resources are not readily available. Due to the high cost associated with space travel, conventional energy production and storage means are not a viable option. To overcome this obstacle, National Aeronautics and Space Administration (NASA) has been working on developing an efficient, effective, energy dense means of storing energy. Storing excess energy during power generation for later use is a critical feature for lunar applications. An important consideration of possible energy storage devices for lunar applications is a high energy density while still being safe and reliable.

Another important consideration is the ability of a storage device to withstand extreme conditions. The extreme lunar conditions are a result of the minimal atmosphere with temperatures ranging from 100 K to 400 K between daylight and darkness [1]. The slow lunar rotation results in a daytime lasting 14 earth days and nighttime lasting 14 earth days. Viable options for energy production includes solar and nuclear. The large period of darkness eliminates the possibility of producing power using solar panels for long periods of time. Nuclear generation is another feasible power source but is unable or limited in power production at the high daylight temperatures. Intermittent power sources expose the need for energy storage during generation for later use. With all storage devices, there are trade-offs of power and energy density, life or charge/discharge cycles, and cost [2]. Flywheels are a

potential energy dense, efficient storage system. Many characteristic features can be implemented to increase the efficiency for lunar applications where it is import to minimize energy waist.

1.2 Flywheel Energy Storage Systems

Flywheels are not a new concept and are used for many mechanical systems. Flywheels in internal combustion engines use the mass of the flywheel to smoothly continue the rotation of the crankshaft. Others are used for continuous drive systems similar to a sheave in belt-driven applications. These systems often use flywheels to transfer energy mechanically through the system. Development of new technologies has arisen to the use of Flywheel Energy Storage System (FESS). FESS's are used to store energy mechanically which is then converted into electrical energy when the motor acts as a generator. The kinetic energy stored in a hollow FESS is given in Equation 1.1:

$$KE = \frac{1}{2} I\omega^2 \quad \text{with} \quad I = \frac{M}{2}(r_i^2 + r_o^2), \tag{1.1}$$

where *KE* is the kinetic energy, *I* is the mass moment of inertia for the flywheel, ω is the angular velocity of the flywheel in rad/s, *M* is the mass of the flywheel, and r_i and r_o are the inside and outside radius respectively for a single material. Many of the FESS's currently in use are hubbed which means the rotor has or is connected to a spinning shaft. If $r_i = 0$, *I* collapses to the moment of inertia for a solid disk.

Currently, FESS's are being used in Uninterruptible Power Supply (UPS) systems, store excess power for later consumption, and mitigate power fluctuations [2] [3]. Large scale models are often used for rapid discharge rates on the order of magnitude of several minutes resulting in a high power density. Despite having a high power density, the large mass and lower angular velocity associated with these models results in a lower energy

density [2]. With the improvement of material technologies, FESS's can operate at higher speeds allowing for a much greater energy density which results from the ω^2 term in Equation 1.1. NASA is interested in the possibility of replacing batteries in space applications if energy density of a FESS can exceed that of batteries [4].

There are many advantages for FESS's that make them a good candidate for the possible replacement of batteries. With the use of Active Magnetic Bearings (AMB) the friction and maintenance can greatly be reduced [5] [6]. The use of an evacuated chamber in conjunction with AMB has the ability to increase the efficiency of the system to 90% [6] [7]. A schematic of a FESS used for an UPS is shown in Figure 1.1 below.

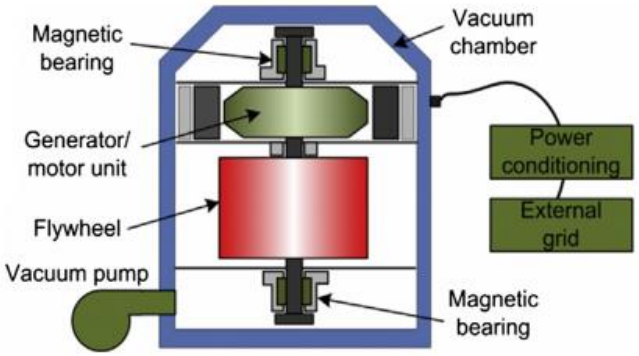

Figure 1.1: Diagram of the key components used for a typical FESS [7]

Unlike batteries with a typical lifetime of 5 years, flywheels have the capability of a lifetime that is approximately 20 years which may be able to offset the large initial startup cost. Chemical batteries have hazardous materials that have to be disposed of where flywheels have nearly none. Currently, FESS's have an energy density in the range of 50-100 Wh/kg however NASA theorizes that FESS's may eventually reach an energy density of 2,700 Wh/kg with an increase of carbon nanofiber technology [4] [7].

1.3 University of Idaho FESS

NASA has provided funding for Phase III of the Steckler Space Grant for the continuation of research into the University of Idaho Flywheel Energy Storage System (UIFESS). The goals for this phase is the extension of research for the use of a hubless, low-speed UIFESS, advancement of education for both undergraduate and graduate students in the STEM workforce, promote interdisciplinary work, develop, test and optimize a high-speed FESS. Concurrently, research is being done by professors and students from Electrical and Computer Engineering, Mechanical Engineering, and Physics departments on the UIFESS. The UIFESS is being designed to store excess power generated from an intermittent power source for later use. The design of the UIFESS will need to simulate the actual operating conditions on the lunar surface to account for possible complication and implementation.

The current low-speed UIFESS is intended to rotate at 1,800 rpm but has been overdesigned to operate at speeds up to 5,000 rpm [8]. At low speeds, much of the analysis can be done for control and debugging issues. As previously stated, the UIFESS is a hubless design. This design decreases the friction losses by removing mechanical bearings. A hubless corresponds to an “inside-out” configuration meaning that the rotor, or flywheel, rotates around a stationary stator. The flywheel consequently needs to be larger which greatly increase the moment of inertia resulting in greater energy storage. An “outside-in” design, incorporating a hub, developed at the NASA Glenn Research Center reached velocities of 60,000 rpm [9]. This flywheel is much smaller than required for actual implementation. The stator is responsible for producing the torque that converts electrical

energy into kinetic energy as well as converting the kinetic energy back to electrical energy. Illustrations of the UIFESS is given in Figure 1.2.

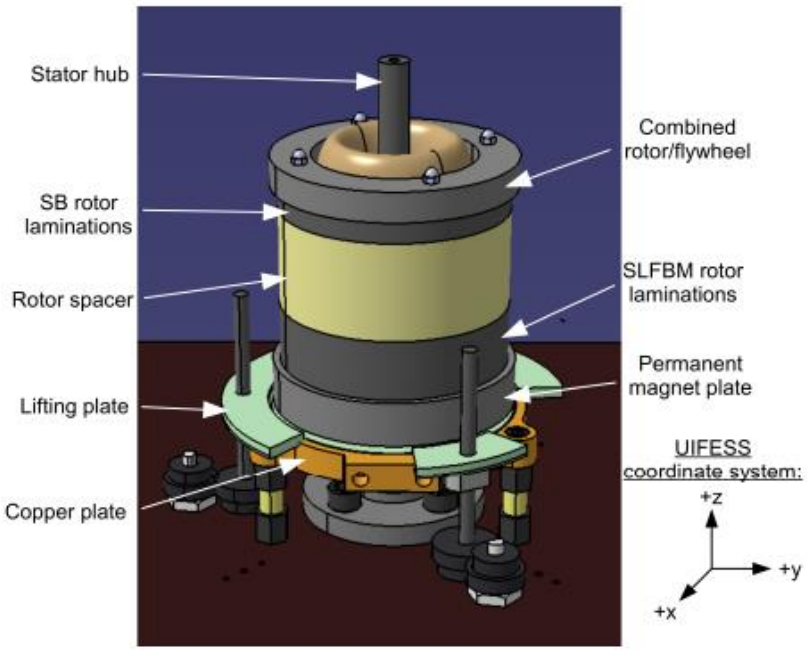

Figure 1.2: Labeled diagram of the UIFESS [8]

To increase the efficiency of the overall system, a Passive Magnetic Bearing (PMB) was implemented to decrease the friction produced from mechanical bearings. The permanent magnetic plate and copper plate embedded with superconductors operates as the PMB for the UIFESS. This frictionless bearing mostly controls the displacement in the z-direction while allowing rotation about the z-axis. A hubless design allows for movement in the x-y plane. Some restoring forces in the x-y plane and resistance to rotation about the x- and y- axis are also applied by the PMB. The PMB operates using high temperature YBCO superconductors and permanent magnets oriented in a Halbach array. Halbach array orients permanent magnetics in specific directions which increases the field gradient and intensity thus increasing levitation forces [10]. These magnets are pressed into a stainless steel plate at the bottom of the rotor labeled as “Permanent magnet plate”. Many FESS’s currently being used operate using AMB to control the radial displacement of a hubbed shaft

for a contactless bearing; analogues to that shown in Figure 1.1. AMB's require electrical power to create levitation force whereas PMB's do not. Use of a PMB allows for a decrease in power consumption during operation increasing the efficiency. The superconductors do however require cooling below a critical temperature for levitation to occur. Critical temperatures for YBCO superconductors are typically ~91 Kelvin [11]. A copper plate and liquid nitrogen are used to cool the superconductors which are size referenced to a guitar pick in Figure 1.3. To control the tilt of the flywheel, a stabilizer bearing, acting as an AMB, is used by delivering radial forces near the top of the flywheel. This induces a corrective moment about the x- and y-axis to re-center the flywheel about the stator. If the flywheel is dynamically balanced, the stabilizing bearing is not needed and becomes a precautionary device.

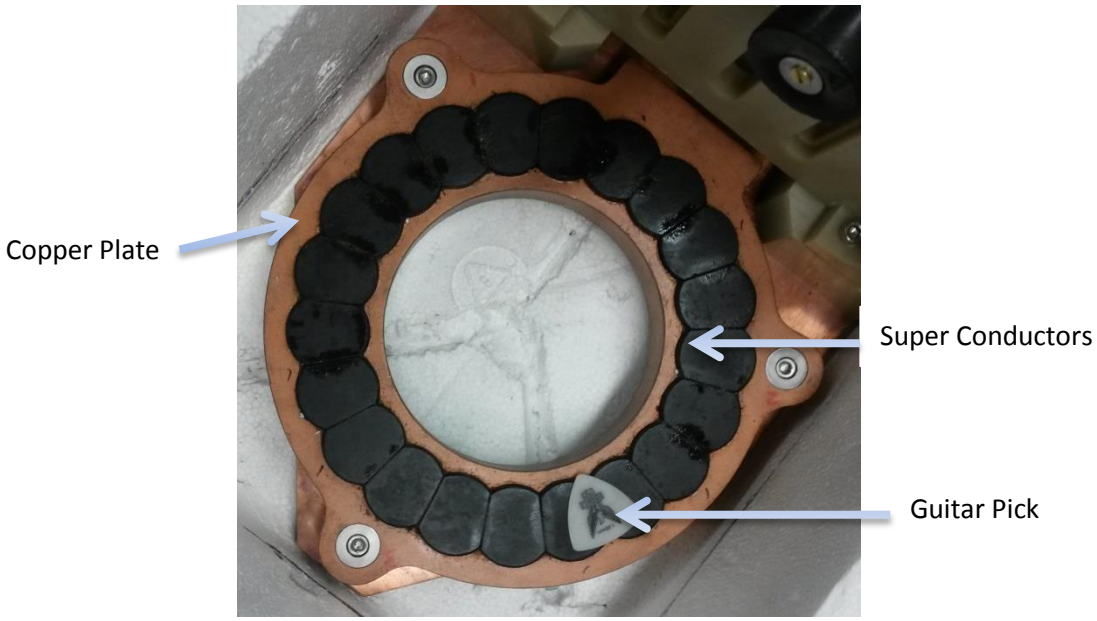

Figure 1.3: Superconductor ring and copper heat conduction plate

The flywheel operates using a Field Regulated Reluctance Machine (FRRM). Operation of FRRM's is done by exciting stator windings in a manner that allows the controlling of the torque and flux to be independent of each other [12]. As the flywheel

accelerates or decelerates, a significant amount of heat is produced in the stator windings. The UIFESS uses cold water that is pumped through the stator shaft to cool the stator windings. For rotation to occur an airgap is required between the rotor and stator. The size of this airgap will limit the forces that can be applied through the stabilizer bearing and the torque that can be induced into the rotor. Applied force is inversely proportional to the square of the airgap size; therefore, the smaller the airgap the larger the applied force.

Introducing the use of iron laminations will increase the efficiency of the overall system. Both the stator and rotor laminations utilize 26 gauge M-36 electrical grade silicon steel. This steel is used for its relatively high magnetic saturation point. Laminations are used to reduce eddy current losses that form perpendicular to the magnetic flux flow when a change in flux occurs. Laminations restrict the size of the eddy current loops thus increasing the efficiency of the system. Geometry used for the stator and rotor laminations used for the FRRM is shown in Figure 1.4. A large magnetic flux penetrates the iron laminations making it desirable to have the ability of a degaussing routine. This is used to eliminate or greatly reduce residual flux in the laminations that occurs from extended use [13]. The FRRM chosen by Wimer utilizes four poles [14]. Six coils per pole results in a total of 24 stator teeth as shown in Figure 1.4 [14]. The stabilizing bearing uses eight coils that are coupled together. Two coils per pole for a total of eight coils are used for the stabilizing bearing as shown in Figure 1.5. Laminations for the AMB are rings with inner and outer radius of 67.49 mm and 95.25 mm respectively. Rotor laminations of the FRRM are the same dimensions for the inner and outer most radii.

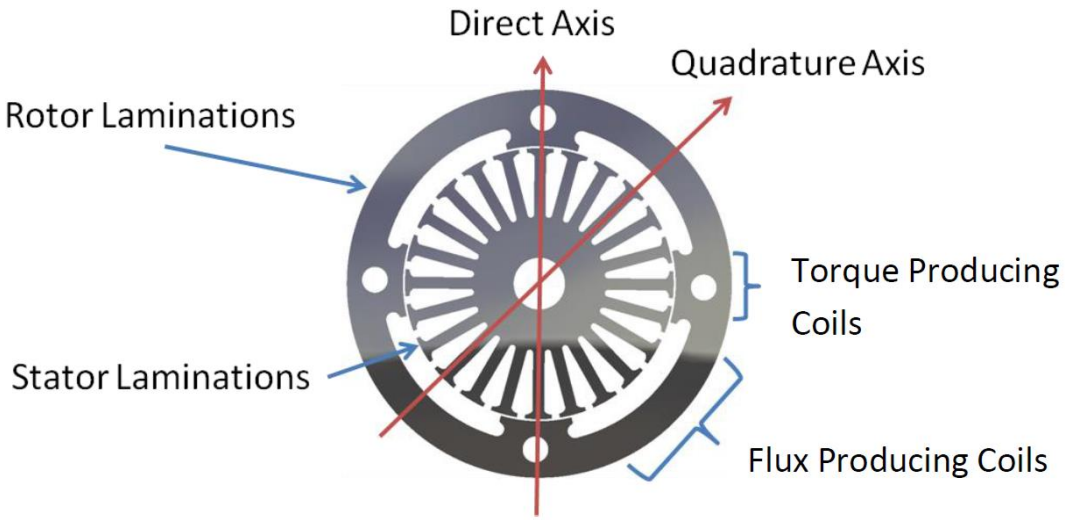

Figure 1.4: Stator and rotor lamination geometry [14]

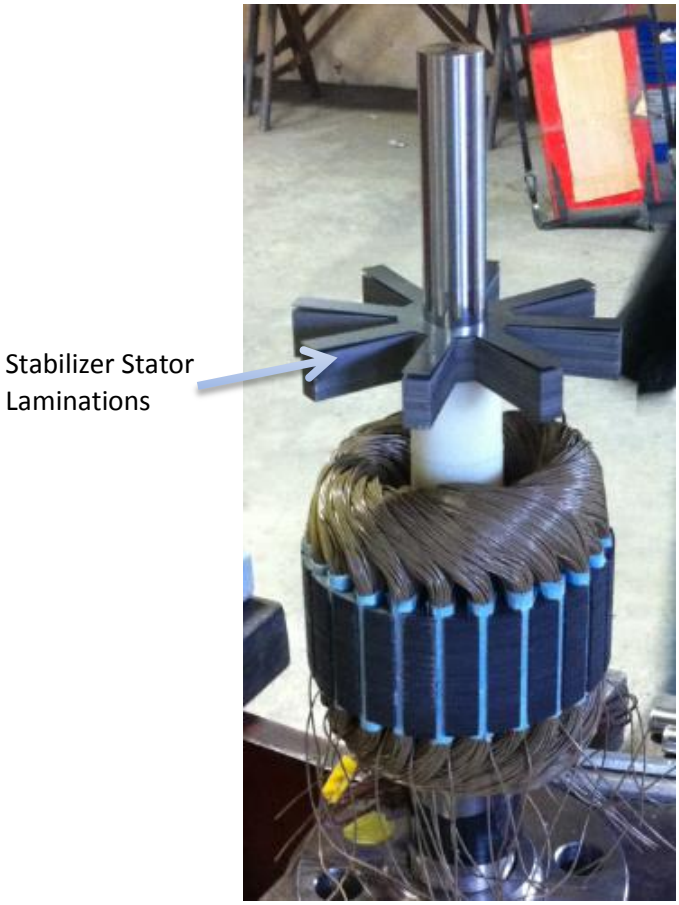

Figure 1.5: Stabilizing laminations and wrapped FRRM laminations

Similar to mechanical bearings, wind drag can be an extensive source of friction loss; especially so at high speeds. A vacuum chamber as shown in Figure 1.6, was selected by Ramus and is capable of an air pressure to 10^{-4} Torr ($1.32X10^{-7}$ atm) [15]. While reducing drag, the vacuum chamber also simulates a portion of the operating conditions of the lunar surface. The use of a vacuum chamber will increase the efficiency during terrestrial operation and testing. Some commercial FESS's use light gases such as helium-air mixtures to reduce losses by up to 42% for a 50% volume of helium to a complete vacuum [16].

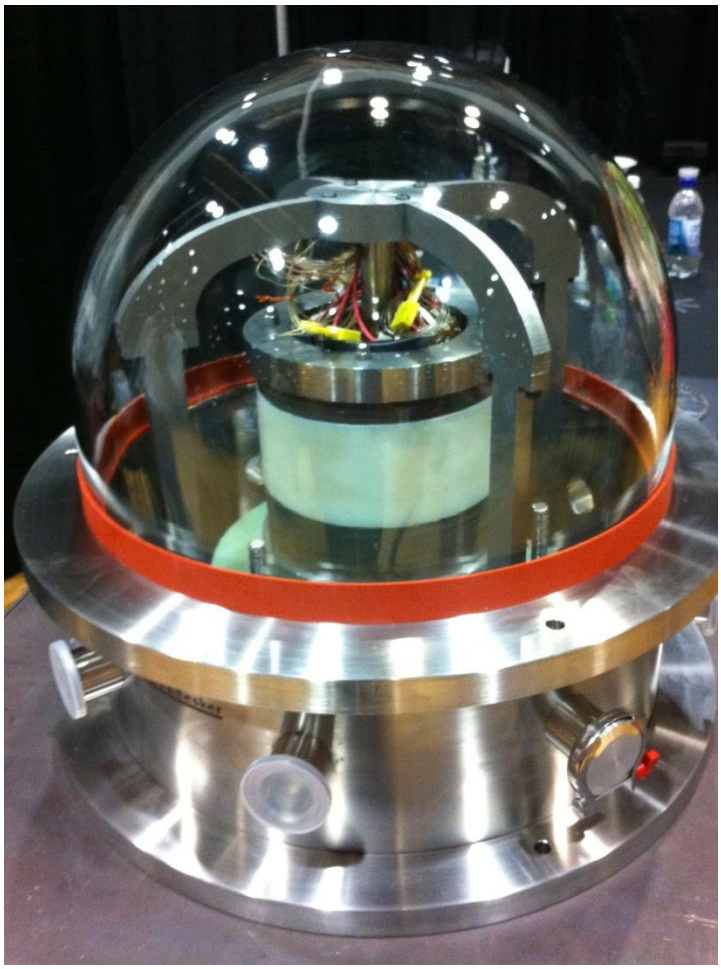

Figure 1.6: UIFESS assembly with vacuum chamber. Power electronics excluded

Eddy current position sensors, which are accurate to a micrometer, measure the radial location of the rotor to determine if the rotor is centered about the stator. These positions are the inputs into the control circuit for the stabilizer bearing. The flywheel being centered is vital for ensuring that contact between the rotor and stator will not occur. Having the rotor centered also ensures that the forces for the FRRM control acts uniformly on the rotor laminations. The position sensors selected by Ramus are used to determine if the airgap needed between the stator and rotor is being maintained [15]. An airgap of 1 mm was determined by Wimer to have an effective applied force for the stabilizing AMB and FRRM [14]. The control and implementation of the AMB to maintain the 1 mm airgap was developed by Kisling [8].

1.4 Thesis objectives

Active rotation of the UIFESS has yet to occur. The current UIFESS is a low-speed, proof-of-concept design to determine the feasibility of a hubless, high-speed FESS. The UIFESS is a critical step in achieving high-speed rotation. From Equation 1.1, high rotational speeds will drastically increase the kinetic energy stored and therefor increase the overall energy density of the FESS. Centrifugal forces at high speeds become very significant; inducing large stresses throughout the rotor. These stresses are a limiting factor for the high-speed UIFESS design.

The primary objective of the work covered in this thesis is to develop a numerical model that defines the stress state of the high-speed UIFESS. This model needs include the needed materials for the FRRM as discussed by Wimer [14]. A numerical model is needed to incorporate the use of wrapped fiber composites. Fiber composites, specifically carbon fiber, can be used for high strength applications while simultaneously reducing weight. High

strength materials are needed to withstand the stresses induced by the high rotational speeds. The model needs to be able to evaluate stresses through multiple physical layers for the iron laminations and possibly multiple composite rings. The anisotropic properties of composites must be incorporated into the model as well.

The second objective is the modification and implementation of the model in an optimization scheme. Two optimization schemes are developed to meet specific requirements. One is to maximize the kinetic energy of the system while the other is to minimize the change in displacement of the inner surface. An intensive optimization scheme allows for the widespread coverage of the design space such that a multiple of design points are considered to find the optimum location. An optimization scheme will consider the strengths of the materials such that failure does not occur. Likewise, consideration of the electrical engineering parameters, such as the stator size, needs to be included.

The final objective is to investigate options for the substitution of the iron laminations and the replacement of the stainless “caps” on the rotor which are currently being used to hold the laminations together. The low strength and the geometry needed to contain the Halbach magnetic array is not able to withstand the rotational speeds for the high-speed UIFESS. For this reason, an alternate method or material is required. A substitute for iron laminations may allow for the removal of the upper stainless steel plate completely and most likely the bottom plate as well. This will contribute to the finalization of the overall rotor design which will later be used to produce a dynamic model for the control algorithm.

1.5 Scope

The work described in this thesis is performed as part of Phase III of the Steckler Space Grant provided by NASA. Phase I resulted in analytical and experimental proof that losses can be reduced during idling periods. It also selected the FRRM as the driving mechanism for the FESS. Phase II is covered in the theses of Kevin Ramus [15], Brent Kisling [8], and Bridget Wimer [14]. Phase II is the design and construction of a low-speed proof-of-concept FESS. This low-speed flywheel is intended for developing control algorithms and to test degaussing routines. Phase III is to evaluate the performance of the low-speed FESS then to design, build, and test the high-speed FESS. The results of Phase II greatly affect Phase III. For this reason, a list is given for the main results from this thesis and that provided by Kevin Ramus [15], Brent Kisling [8], and Bridget Wimer [14].

In this thesis:

- Discussion of composite behaviors
- Development and modification for an axisymmetric rotor design
- Optimization schemes for the minimization of the inner rotor radius and maximization of energy

By Kisling [8]:

- AMB control algorithm
- Stabilizer bearing design
- FRRM control algorithm framework

By Ramus [15]:

- UIFESS component selection including microcontrollers, vacuum chamber, power amplifier, and sensors

- Printed circuit boards for interfacing power electronic components
- Investigation of the speed capabilities of power electronics

By Wimer [14]:

- Design of the FRRM
- Dynamic model and simulation for the UIFESS
- Derivation of AMB force expressions

The overview of analysis and behaviors of composite materials is covered in Chapter 2 of this thesis. The formulation of the model used to approximate the stresses in the rotor is located in Chapter 3. This chapter will also give an overview of the modification made to the model used for the optimization schemes. Formulation of the optimization schemes used is given in Chapter 4; one for the kinetic energy and another for displacement. Summary, recommendations for future work, and conclusions is presented in Chapter 5.

Chapter 2. Composite Overview

2.1 Composites

Composite materials are a combination of two or more other materials. The application of composite materials is extremely vast and is found anywhere between sports equipment to turbine blades. Composite materials often offer higher strength to weight ratios while maintaining the ability to be customized for strength, weight, and stiffness [17]. The aerospace industry has been an extensive consumer of composite materials. These composite materials include fiber composites such as carbon fiber and metal composites such as hybrid titanium composite [18]. Two main types of composite materials exist: particulate and fibrous. Both fiber and particulate composites use a matrix material to suspend the particulates or fibers. High strengths associated with fiber composites results from a very high-strength fiber used with a low strength matrix. Fibrous composites are typically more effective than particulate composites when associated with the strength of the material [19]. This discussion on composites is weighted towards the use of fibrous materials because of their high strengths.

Fiber composites use very small fibers implanted in a matrix material. Typically, the fibers are high-strength, denser materials and the matrix has lower strength and density. A majority of the force in the composite is supported by the fiber while the matrix material is used to hold everything together. Typical matrix materials include polymers, metals, and ceramics. Polymers are the most widely used matrix material and operate typically at lower temperatures. Metal and ceramic matrix materials are generally used at higher temperatures or when increased stiffness is required. Compatibility between the fiber and matrix material is needed to ensure the bond strength, either physically or chemically, is susceptible [19].

It was shown by Griffith that as the diameter of a rod or fiber gets smaller the strength increases [20]. Extrapolating his test results shows that for large diameters the strength is that of the bulk properties but for smaller diameters the strength approaches the strength of the atomic bonds. This occurs because at a smaller diameter, the probability of microstructural discontinuities is smaller [20]. It is therefore desirable to have very small fibers in high strength applications. This is comparable to the size effect used in the stress-life fatigue analysis for reducing the fatigue limit [21].

Four main types of fiber-reinforced composite exist; each with its own particular application. The four types, shown in Figure 2.1, are continuous fiber (Figure 2.1a), woven fiber (Figure 2.1b), chopped fiber (Figure 2.1c), and hybrid (Figure 2.1d) [19].

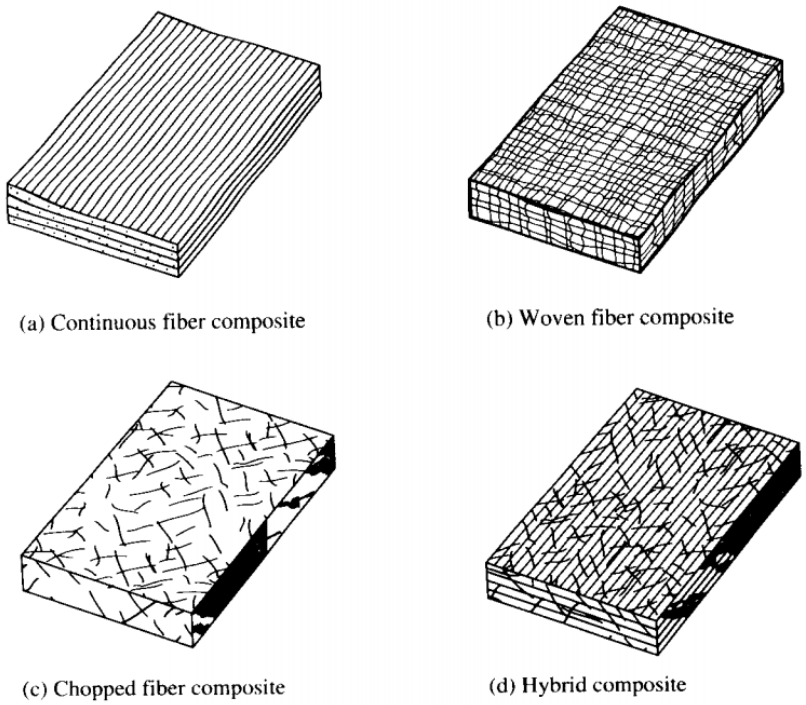

Figure 2.1: Types of fiber-reinforced composites [19]

Continuous fiber composites use fibers aligned in similar directions to form lamina. Lamina is a sheet of a composite material that typically has similar properties throughout the sheet. Continuous fiber laminas generally have high stiffness and strengths aligned with the

fiber and much weaker properties in the other directions. Laminates are formed by adhering multiple lamina that are oriented differently and/or have different physical properties. This is analogues to gluing thin wood sheets together. Lamina orientations are determined by the loading of the laminate. Laminates offer high strength properties in the direction needed while decreasing weight. Delamination, which is typically characterized by the strength of the matrix material, is a major problem that exists with laminates [19]. Delamination is driven by the interlaminer shear stress. This shear stress results from one lamina deforming at different rates than the adjacent laminas [19]. Lamina stiffness and orientation are the main contributors to interlaminer shear stress. Woven fiber composites reduce the possibility of delamination. The trade-off for this, however, is a reduction in strength and stiffness from single directionally aligned fibers. The fiber direction in woven composites is no longer always aligned. This reduces the strength and stiffness in that direction but increases it in the other direction.

Chopped fiber composites use relatively short fibers randomly located throughout the matrix material. This type of composite is cheap and more suited for high-quantity manufacturing. The effective strength and stiffness of chopped fiber composites are significantly reduced compared to continuous fiber composites. The fibers in chopped composites typically fail in shear rather than tensely like with continuous fibers. Shear loading of the fiber occurs from how the matrix material distributes the load to the fiber [19]. When these composites are loaded the Hybrid composites are a mixture the other three types or a combination of multiple fiber types.

Applications that require a component to be loaded predominately in bending often use foam or honeycomb cores sandwiched by fiber laminates [19]. Stress for a material in

bending is a function of the bending moment, area moment of inertia, and the distance from the neutral axis. The analysis of composite laminates in bending is more complicated yet is still a function of the perpendicular distance from the neutral axis of the beam to the location of interest. This means that the stress for a component in pure bending is much less towards the center of the beam and zero at the neutral axis. Low stresses near the center allows for lighter, cheaper, inferior materials to be used at the center of the beam or component. Using a foam or honeycomb core with lamina on either side is known as a sandwiched configuration. The sandwiched configuration results in structure with a high flexural stiffness-to-weight ratio. The multiple possible combinations of fiber and matrix materials and laminate/structural layup make fiber composite design flexible and customizable for numerous applications.

2.2 Continuous Fiber Mechanics

The stress state for composite materials is determined by the strain at a point and the stiffness matrix. Unlike isotropic materials, composite materials have different material properties in different directions. Different material properties are influenced by fiber alignment. Fiber materials may also have anisotropic behavior from affects at the microscopic level. For a fully elastic anisotropic material the stress state is defined as Equation 2.1 [19]:

$$\boldsymbol{\sigma} = \boldsymbol{C} * \boldsymbol{\varepsilon}, \tag{2.1}$$

where $\boldsymbol{\sigma}$ is the stress state at a point, $\boldsymbol{C}$ is the stiffness matrix defined as $[C_{ij}]$ where i,j = 1, 2,…,6, and $\boldsymbol{\varepsilon}$ is the strain vector at a point. Aligned fiber composites typically behave such that the material properties with respect to three mutually orthogonal planes or directions [19]. Typically these principal planes are labeled as (123). This behavior is known as

orthotropic. Specially orthotropic is when the non-principal directions (xyz) is oriented such that one of the principle and non-principal directions are aligned. The stiffness matrix for specially orthotropic materials is represented below [19]:

$$\boldsymbol{C} = \begin{bmatrix} C_{11} & C_{12} & C_{13} & 0 & 0 & 0 \\ & C_{22} & C_{23} & 0 & 0 & 0 \\ & & C_{33} & 0 & 0 & 0 \\ & & & C_{44} & 0 & 0 \\ & SYM & & & C_{55} & 0 \\ & & & & & C_{66} \end{bmatrix}. \qquad 2.2$$

Composite macroscopic lamina properties change with respect to which direction is being considered. For instance, the stiffness of the lamina along the direction of fiber is different than that perpendicular to the fiber orientation. For this reason the longitudinal and transverse modulus are not equivalent. Similarly, Poisson's ratios are directionally dependent. The modulus of elasticity in the 1 and 2 direction are E_1 and E_2 respectively. The property ν_{12} is considered the major Poisson's ratio while ν_{21} is called the minor Poisson's ratio. The difference is a result of loading. For $\nu_{ij} = -\varepsilon_j/\varepsilon_i$, *i* is the load direction and *j* is the direction of the strain that is being affected. For isotropic materials, the direction of loading does not affect the property therefore $\nu_{12} = \nu_{21}$. Although the major and minor Poisson's ratios are different, they are related to each other by $\nu_{ij}/E_i = \nu_{ji}/E_j$ [19].

In Equation 2.1, the stiffness matrix ***C*** is a function of the material properties and relates strain to stress. The compliance matrix **S** is used to correlate the stress to strain and is more easily correlated to the lamina properties. The relation between **S**, **σ**, and **ε** is given in Equation 2.3 [19].

$$\begin{Bmatrix} \varepsilon_1 \\ \varepsilon_2 \\ \varepsilon_3 \\ \gamma_{23} \\ \gamma_{31} \\ \gamma_{12} \end{Bmatrix} = \begin{bmatrix} \frac{1}{E_1} & \frac{-\nu_{21}}{E_2} & \frac{-\nu_{31}}{E_3} & 0 & 0 & 0 \\ \frac{-\nu_{12}}{E_1} & \frac{1}{E_2} & \frac{-\nu_{32}}{E_3} & 0 & 0 & 0 \\ \frac{-\nu_{13}}{E_1} & \frac{-\nu_{23}}{E_2} & \frac{1}{E_3} & 0 & 0 & 0 \\ 0 & 0 & 0 & \frac{1}{G_{23}} & 0 & 0 \\ 0 & 0 & 0 & 0 & \frac{1}{G_{31}} & 0 \\ 0 & 0 & 0 & 0 & 0 & \frac{1}{G_{12}} \end{bmatrix} \begin{Bmatrix} \sigma_1 \\ \sigma_2 \\ \sigma_3 \\ \tau_{23} \\ \tau_{31} \\ \tau_{12} \end{Bmatrix} \quad 2.3$$

where G_{ij} is the shear modulus, γ_{ij} is the shear strain resulting from the shear stress τ_{ij}. Compliance matrix, $\boldsymbol{S}$, and stiffness matrix, $\boldsymbol{C}$, are related by $\boldsymbol{S}^{-1} = \boldsymbol{C}$. The relationship between the shear modulus, elastic modulus, and Poisson's ratio is given as:

$$G_{ij} = \frac{E_i}{2(1+\nu_{ji})}. \quad 2.4$$

Many specially orthotropic lamina are represented in a 2D stress state otherwise known as plane stress. Plane stress assumption results in $\sigma_3 = \tau_{23} = \tau_{31} = 0$ from Equation 2.3. Most uses of orthotropic lamina result in the load directions not being aligned with the principle axis which is referred to as generally orthotropic. This alignment is shown in Figure 2.2. A coordinate transformation matrix is required to rotate the stresses and strains from one coordinate system to another. The transformation matrix in for rotating from the x-y coordinate system to the 1-2 coordinate system is defined below [19]:

$$\boldsymbol{T} = \begin{bmatrix} \cos^2(\theta) & \sin^2(\theta) & 2\cos(\theta)\sin(\theta) \\ \sin^2(\theta) & \cos^2(\theta) & -2\cos(\theta)\sin(\theta) \\ -\cos(\theta)\sin(\theta) & \cos(\theta)\sin(\theta) & \cos^2(\theta) - \sin^2(\theta) \end{bmatrix}, \quad 2.5$$

where θ is the angle between the x-axis and the 1-axis.

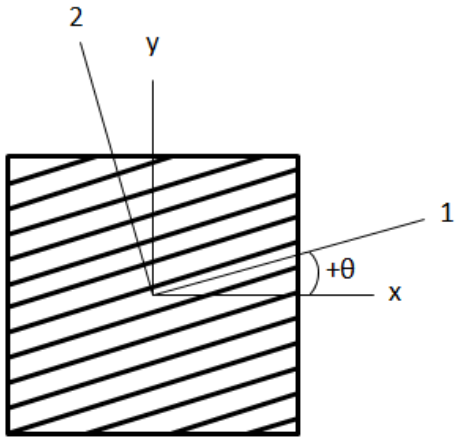

Figure 2.2: Generally orthotropic lamina principle and load alignment

Material choices, alignment, and volume factions give a large range of flexibility in the design composite materials. A large range of flexibility makes it desirable to characterize the macroscopic properties of a composite without extensive testing for individual properties. Calculating elastic and shear moduli and Poisson's ratios of aligned continuous fiber composites requires the similar properties of the fiber, matrix material, and the fiber volume fraction. The following analysis is based on the following qualifications [19]:

- Fibers are continuous and aligned
- Fiber volume fraction is constant throughout the composite
- Fiber and matrix materials are assumed to be linear elastic
- Perfect bonding between the fibers and matrix is assumed
- Fiber and matrix are assumed to be homogeneous
- Lamina is assumed to be macroscopically assumed to be homogeneous, linearly elastic and orthotropic
- Stresses, strains, displacements, and dimensions are assumed constant for a small Representative Volume Element (RVE)
- The matrix material is assumed to be isotropic

The elastic modulus in the fiber direction and the major Poisson's ratio is shown to be $E_1 = \Sigma E_i v_i$ and $\nu_{12} = \Sigma \nu_{12} v_i$ where v_i is the volume fraction of the individual components [19]. The transverse and shear modulus equation (Equation 2.6) was derived by Tsai and Hahn and correlated to experimental data for verification [19].

$$\frac{1}{E_2, G_{12}} = \frac{1}{v_f + \eta_2 v_m}\left[\frac{v_f}{E_{f2}, G_{f12}} + \frac{\eta_2 v_m}{E_m, G_m}\right] \quad \text{with} \quad \eta_2 = 0.5, \qquad 2.6$$

where E_2 is the effective transverse modulus for the composite, E_{f2} is the is the transverse modulus of the fibers, E_m is the modulus for the matrix material, and v_f and v_m are the volume fractions for the fiber and matrix respectively. The overall composite shear modulus, G_{12}, is calculated using G_{f12} and G_m which are the shear modulus for the fiber and matrix material respectively. While it is important to know how a composite will deform for an applied stress, it is also to know the extent of the stress that will result in failure.

Approximating the physical strength of a composite can be a more difficult process than the stiffness. For the longitudinal strength, the method used to calculate the strength is dependent upon which material has a lower maximum strain. Most engineering fiber composites have a failure strain that is less than the matrix material. Once a fiber failure occurs, the load supported by the fiber transfers to the matrix material. In most cases, the matrix has a lower strength therefore fiber failure means failure for the composite.

A composite with a fiber failure strain that is less than the critical matrix strain results in the matrix supporting a portion of the stress. This stress is equivalent to the product of the strain of the fiber and the stiffness of the matrix. The strength addition from the matrix at fiber failure and is denoted as $s_{mf1}^{+} = E_m e_{f1}^{+}$ where e_{f1}^{+} is the maximum longitudinal tensile strain for the fiber. The equation for the overall longitudinal tensile strength for a lamina as a function of the volume fraction becomes [19]:

$$s_L^+ = s_{f1}^+ v_f + s_{mf1}^+ (1 - v_f), \quad 2.7$$

where s_L^+ is the longitudinal strength of the lamina and s_{f1}^+ is the strength of the fiber. Some composites have matrix materials that have a lower allowable strain than the fiber. For these materials, the longitudinal strength of the lamina is found using Equation 2.8 [19]:

$$s_L^+ = s_{fm1}^+ v_f + s_{m1}^+ (1 - v_f) \quad \text{where} \quad s_{fm1}^+ = E_{f1} e_{m1}^+. \quad 2.8$$

Transverse and shear strength of a continuous fiber lamina is largely dependent on the matrix material used. Analysis for the two strengths is very similar. These strengths are much lower and often a limitation in laminate composites. The transverse strength can be found using Equations 2.9 and 2.10 and the shear strength is found using Equations 2.11 and 2.12 [19]:

$$s_T^+ = \frac{E_2 s_m^+}{E_m F}, \quad 2.9$$

$$F = \frac{1}{\frac{d}{s}\left[\frac{E_m}{E_{f2}} - 1\right] + 1}, \quad 2.10$$

$$S_{LT} = \frac{G_{12} s_m^+}{G_m F_s}, \quad 2.11$$

$$F_s = \frac{1}{\frac{d}{s}\left[\frac{G_{m12}}{G_{f12}} - 1\right] + 1}. \quad 2.12$$

The effective transverse modulus E_2 is found using Equation 2.6. F is the strain concentration factor with d representing the fiber diameter and s representing the distance between the fibers. G_{12} is the effective shear modulus found in Equation 2.6. Fs is the in-plain shear strain concentration factor and G_{m12} is the average matrix in-plain shear modulus.

2.3 Randomly Oriented Chopped Fiber Mechanics

Stiffness properties for randomly oriented chopped fibers composites are estimated based on the analysis of aligned short fibers. Aligned short fiber composites have better strength and stiffness properties than randomly oriented fiber composites. Alignment of short fibers is a difficult manufacturing process. The macroscopic longitudinal modulus is affected by the use of discontinuous short fibers; however, Halpin concluded E_2, G_{12}, and v_{12} were marginally affected by the fiber length [19]. The resulting equation for the longitudinal modulus is given in Equation 2.13:

$$\frac{E_1}{E_m} = \frac{1+\xi\eta v_f}{1-\eta v_f}, \quad \eta = \frac{\left(\frac{E_{f1}}{E_m}\right)-1}{\left(\frac{E_{f1}}{E_m}\right)+\xi}, \quad \text{and} \quad \xi = \frac{2L}{d}, \tag{2.13}$$

where L is the length of the fiber, d is the diameter of the fiber, and E_{f1} is the longitudinal modulus of the fiber. Marginal effect on the transverse modulus allows for the use of the improved inverse rule of mixtures as given in Equation 2.14 [19]. Given the results of Equations 2.13 and 2.14, the averaged isotropic properties can be found using the Tsai and Pagano equation (Equation 2.15).

$$E_2 = \left[\left(1-\sqrt{v_f}\right) + \frac{\sqrt{v_f}}{1-\sqrt{v_f}\left(1-\frac{E_m}{E_{f2}}\right)}\right] \tag{2.14}$$

$$\tilde{E} = \frac{3}{8}E_1 + \frac{5}{8}E_2 \quad \text{and} \quad \tilde{G} = \frac{1}{8}E_1 + \frac{1}{4}E_2. \tag{2.15}$$

Poisson's ratio for the randomly oriented, short fiber composite can be found by inputting $\tilde{E}$ and $\tilde{G}$ from Equation 2.15 into Equation 2.4. The relationship between fiber volume fraction, the ratio between $\tilde{E}$ and E_1, and the ratio between E_f and E_m is shown in Figure 2.3 [19]. This gives a visual image for the effect of the fiber modulus on the effective modulus for the randomly oriented, short fiber composite.

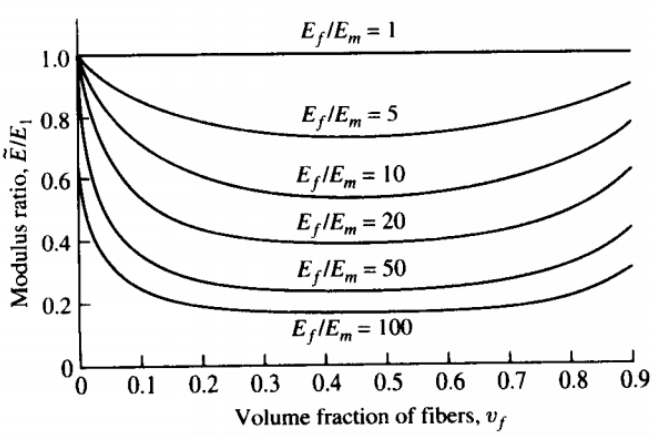

Figure 2.3: Effect of short fiber modulus on the effective modulus [19]

Strength analysis for short, randomly oriented fibers is based on continuous the continuous fiber analysis yet is much than continuous fiber analysis. A representative volume element, like the one shown in Figure 2.4, of a single short fiber in an off-axis orientation is analyzed. Integrating the RVE over all possible orientations results in an average strength for randomly oriented, short fiber composites [19]. Chen (Equation 2.16) and Lees (Equation 2.17) both developed approximations for the strength of the composite as a function of the strengths for a continuous fiber composite [22] [23]:

$$\tilde{\sigma}_x = \frac{2s_{LT}}{\pi}\left[2 + \ln\frac{\psi s_L^+ s_T^+}{s_{LT}^2}\right] \qquad 2.16$$

$$\tilde{\sigma}_x \cong \frac{2s_{LT}}{\pi}\left[1 + \frac{s_T^+}{s_{mf1}} + \ln\frac{s_{mf1}s_T^+}{s_{LT}^2}\right], \qquad 2.17$$

where s_{LT} is the shear strength from the continuous fiber analysis (Equation 2.11), ψ is an efficiency factor which is assumed to be one when unknown or estimated as a percent of the effective randomness. The variables s_L^+ (Equation 2.7) and s_T^+ (Equation 2.9) are for a continuous fiber composite. Equations 2.16 and 2.17 are significantly influenced by the shear strength as a result of matrix supporting much of the load. Well-defined fiber strengths and stiffness properties are needed to compute the lamina stiffness and strengths using equations introduced in sections 2.2 and 2.3 of this thesis.

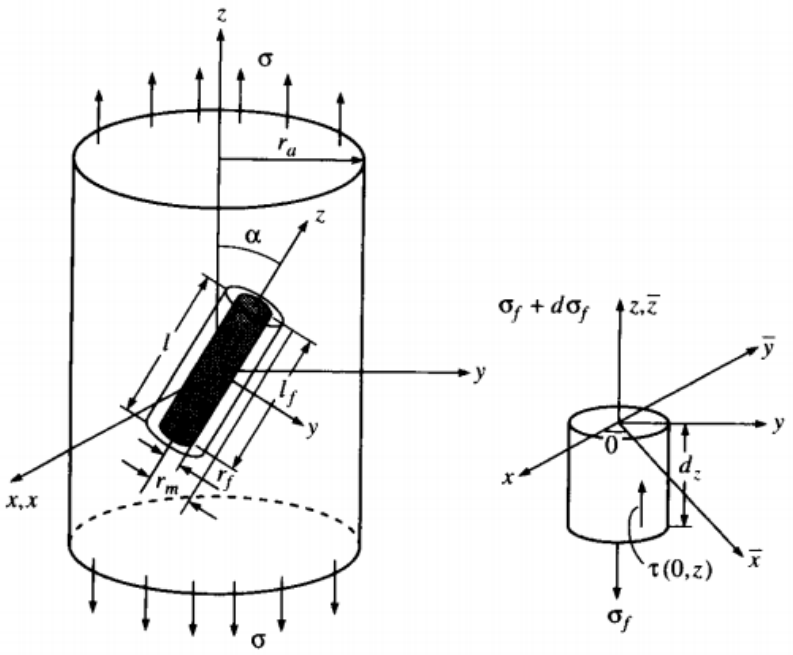

Figure 2.4: RVE for off-axis short fiber [19]

2.4 Failure Criterion

Three main types of failure criterion exist for composite laminas. These are the maximum stress, maximum strain, and Tsai-Hill criterions [19]. The Maximum Stress Criterion states that if a stress in the lamina reaches the maximum stress of the component, whether tensile, compressive, or shear then failure will occur. Maximum Strain Criterion states that if the strain in the lamina reaches the maximum strain of the component then failure will occur. The Tsai-Hill failure surface for plain stress is a function of the biaxial stresses and the shear stress. Tsai-Hill Criterion was developed as a modification to the commonly used maximum distortional energy criterion; otherwise known as the von Mises Criterion [19]. The three failure criterions are shown in σ_1, σ_2 space in Figure 2.5. The load direction is distinguished using (+) for tensile loading and (-) for compressive loading and the strength is signified by *s* with *T* and *L* signifying the fiber direction.

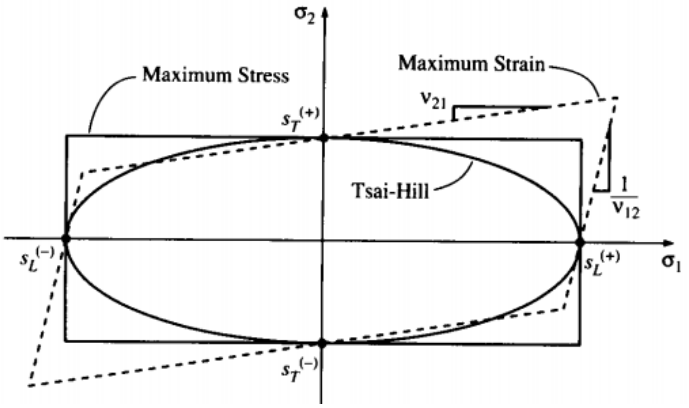

Figure 2.5: Maximum stress, maximum strain, and Tsai-Hill failure criterions [19]

Maximum Stress Criterion creates the rectangle shape shown in Figure 2.5. The interaction between stress components is not incorporated in this failure criterion. It has been shown to be accurate for uniaxial loadings as shown in Figure 2.6 [19]. Maximum Strain Criterion creates a parallelogram shape. This incorporates added strain in biaxial loading scenarios. Most physical evidence does not support this criterion at the intercepts of the parallelogram which can be seen in Figure 2.6 [19]. The Tsai-Hill Criterion is a continuous function which accounts for loading in the 1 and 2 directions and the shear stress as shown in Equation 2.18)[19]:

$$\frac{\sigma_1^2}{s_L^2} - \frac{\sigma_1\sigma_2}{s_L^2} + \frac{\sigma_2^2}{s_T^2} + \frac{\tau_{12}^2}{s_{LT}^2} = 1 \quad . \qquad 2.18$$

The directions are not specified in the Tsai-Hill equation because the loading can be either positive or negative. If the left-hand portion of Equation 2.18 is greater than one, then failure has occurred according to this criterion. This failure criterion is a reasonable fit for many composite materials [19] and more conservative as shown in Figure 2.6. The fourth failure surface in Figure 2.6 is the Tsai-Wu Criterion. This is shown to be more accurate but requires strength tensors that are experimentally determined [19].

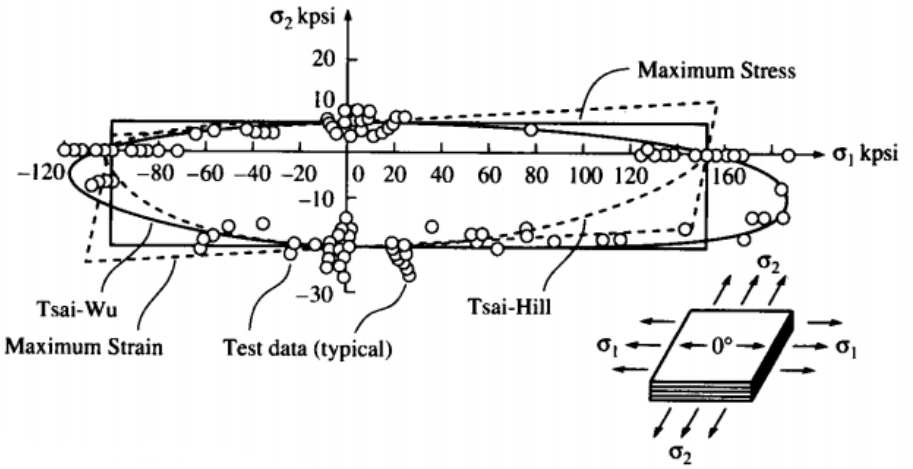

Figure 2.6: Comparison of the maximum stress, maximum strain, and Tsai-Hill failure criterions [19]

Chapter 3. Model

3.1 Model Development

This chapter introduces the development of a model that calculates the stresses and displacements in the high-speed flywheel energy storage system. These outputs are necessary for their use in understanding and defining the feasible design region. The optimal configuration and size of the flywheel is located in this region. Stress outputs determines approximately when the iron laminates will experience yielding. The displacement determines if the 1 mm airgap can be maintained within the reasonable range required for the FRRM to operate [14].

The stress state of rotating isotropic materials is well understood [24]. The stress equations are functions of the Poison's ratio, density, and the angular velocity. These equations are used to describe an isotropic, homogeneous material undergoing elastic deformation. These equations cannot be used to calculate the stress state of an anisotropic, nonhomogeneous material.

The study of composite flywheels has become more abundant with newfound applications. This includes the study of solid rotating composite disks. Rajeev Jain, et al, derived an analytical result of a solid, constant thickness, uniform strength, anisotropic disc [25]. Their analysis also examined a radially varying modulus disc. Both cases were compared with a Finite Element Analysis (FEA) for validity. Similarly, Xu-Long Peng and Xian-Fang Li studied the stress distribution of a functionally graded solid disk [26]. A functionally graded composite disk is one where the properties vary radially. An example of this would be a disc that the fiber volume fraction increases radially. The benefit of a functionally graded material is the reduction large stress discontinuities that occur when

rings with different physical properties are present. Multiple physical rings is an example of a nonhomogeneous rotor that excludes the use of the isotropic stress state equations.

The design and testing of a FESS with dome-type hub matched with reasonable precision of a FEA model [27]. A cross-sectional view of the rotor is shown in Figure 3.1. Their rotor design was able to match radial growth to prevent separation. The 325 kg flywheel was tested to a maximum speed of 17,000 rpm at which the stored energy was 50 kWh.

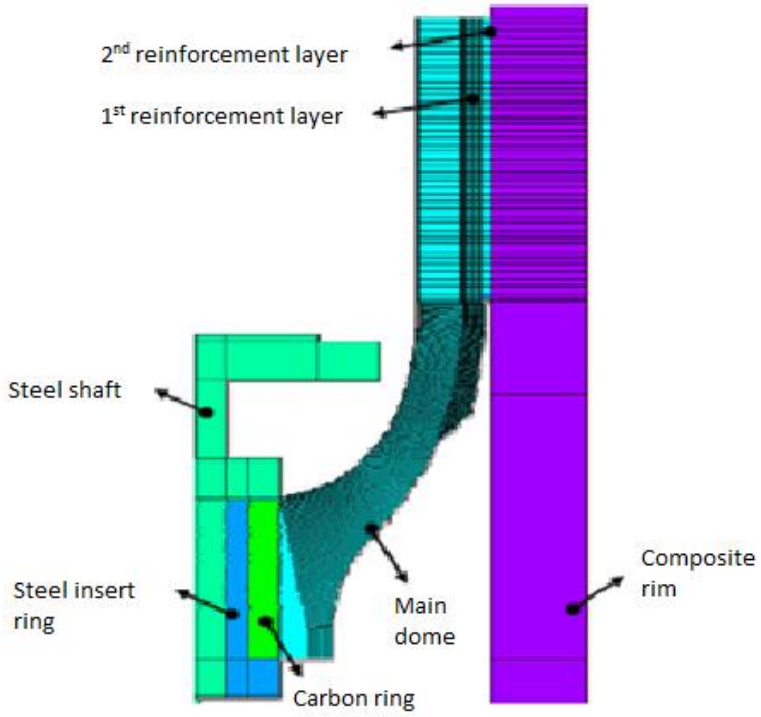

Figure 3.1: Cross-sectional design 50 kWh FESS with a dome-type hub [27]

When helically wrapping a disc with a ply orientation of ±θ in the r-z plane, the resulting structure has a mosaic pattern as shown in Figure 3.2 [28]. Uddin, et al, modeled the flywheel as being hollow and the orientations as being orthotropic. Fiber-reinforced composites often behave in an orthotropic manner which is a special case of anisotropy. Orthotropic materials have properties that differ with respect to the three orthogonal axes.

Their results compared the stress distribution in the mosaic pattern to the typical analysis which is that of a laminated shell. The analysis conducted used a finite element model with different mosaic patterns.

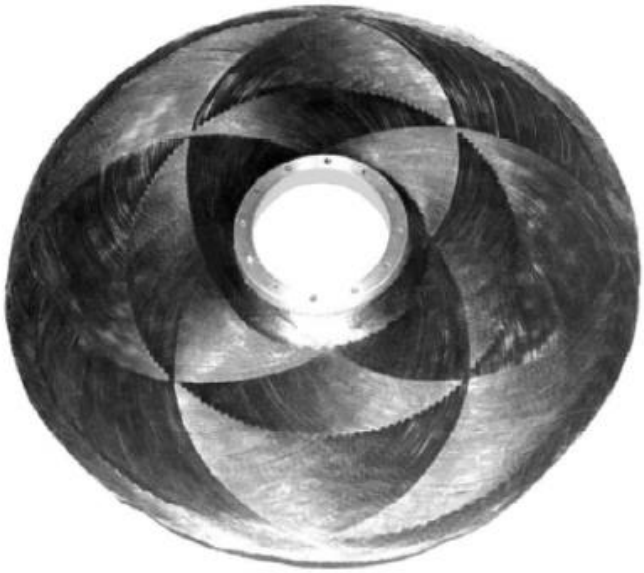

Figure 3.2: Mosaic pattern resulting from ±θ continuous fiber helical wrapping [28]

A non-axisymmetric layered composite disc analysis was developed by Tahani, et al [29]. Their model includes the shear stress present when the flywheel is no longer axisymmetric. Out-of-plane and shear composite properties are often times not readily available from composite manufactures. The use of the non-axisymmetric model would require many estimated or physically tested properties for the model to operate.

Analysis of a single composite material would not incorporate the use multiple materials, such as iron laminations, that are needed for the flywheel to operate. The functionally gradient analysis also excludes the iron laminations therefore excluding that analysis. Design and testing of a design incorporating a dome shape hub gave good results as compared to a FEA model. Use of a dome-shaped hub removes this as possible design method. Implementing a mosaic type pattern using an FEA model could be a possible option

for the final design. Because a FEA was used in the mosaic analysis, the multiple materials and orientations could potentially be incorporated into the FEA. The ability to iteratively solve for a rotor design is extremely computationally expensive. The final flywheel design will require a full finite element analysis to ensure localized yielding will not occur. These limitations resulted in the use of an axisymmetric model developed by Sung K. Ha, et al.

This axisymmetric model chosen is developed using a plain strain assumption for an axisymmetric flywheel [30]. The flywheel is assumed to be thick enough for this assumption to be valid. This model has the capability of having multiple physical rings. Physical rings are defined as different material. A schematic of a similar FESS with multiple physical rings is shown Figure 3.3. However, instead of utilizing permanent magnets a material capable of transferring magnetic flux will be used for the FRRM. Laminations for the UIFESS will be considered one physical ring. The addition of other materials would add to the total number of physical rings. Multiple rings may be needed to increase the strength of the rotor and/or for construction of the final design in a high-speed application.

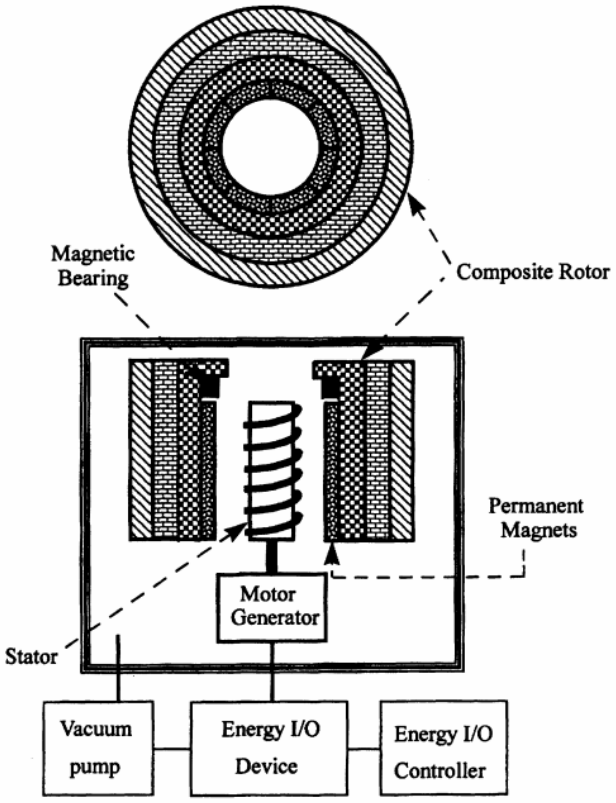

Figure 3.3: Composite flywheel diagram for FESS with multiple rings [30]

The stress state the model developed by Sung K. Ha, et al can then be described by the following relationship:

$$\begin{pmatrix}\sigma_\theta\\ \sigma_z\\ \sigma_r\end{pmatrix}=\begin{bmatrix}Q_{11} & Q_{12} & Q_{13}\\ Q_{12} & Q_{22} & Q_{23}\\ Q_{13} & Q_{23} & Q_{33}\end{bmatrix}\begin{pmatrix}\varepsilon_\theta\\ \varepsilon_z\\ \varepsilon_r\end{pmatrix} \quad \text{with} \quad \boldsymbol{Q}=\begin{bmatrix}\frac{1}{E_\theta} & \frac{-\nu_{\theta z}}{E_z} & \frac{\nu_{\theta r}}{E_r}\\ \frac{\nu_{\theta z}}{E_\theta} & \frac{1}{E_z} & \frac{\nu_{rz}}{E_r}\\ \frac{\nu_{\theta r}}{E_\theta} & \frac{\nu_{rz}}{E_z} & \frac{1}{E_r}\end{bmatrix}^{-1}, \tag{3.1}$$

where $\boldsymbol{\sigma}$ and $\boldsymbol{\varepsilon}$ are the stress and strain vectors and $\boldsymbol{Q}$ is the stiffness matrix for the axisymmetric material. These axes are defined as θ-z-r. Directions 1, 2, and 3 from Equation 3.1 correspond to θ, z, and r respectively. Stiffness matrix $\boldsymbol{Q}$ from Equation 3.1 is a simplification from Equation 2.3 resulting from normal stresses only inducing normal strains therefore neglecting shear strains and stresses [19]. The axisymmetric strains are defined as:

$$\varepsilon_\theta = \frac{u_r}{r} \quad \text{and } \varepsilon_r = \frac{du_r}{dr}, \tag{3.2}$$

where ε_θ and ε_r are the circumferential and radial strains respectively and u_r is the radial displacement at a given r.

To solve for $\boldsymbol{\sigma}$ numerically, the flywheel with multiple physical rings is divided into numerical rings. Numerical rings are implemented to increase the accuracy of numerical model. As the thickness of the numerical rings approaches zero the more precise the numerical solution. The stress and strain vectors are then used to develop the equations for radial displacement u_r and normal stress σ_r:

$$u_r = -\rho\omega^2\varphi_0 r^3 + C_1\varphi_1 r^\kappa + C_2\varphi_2 r^{-\kappa} \tag{3.3}$$
$$\sigma_r = -\rho\omega^2\varphi_3 r^2 + C_1 r^{\kappa-1} + C_2 r^{-\kappa-1}, \tag{3.4}$$

where ρ is the density of the physical ring, C_1 and C_2 are unknown constants which are solved for using boundary conditions. The values κ and ϕ_i are defined with respect to the material properties:

$$\varphi_0 = \frac{1}{(9-\kappa^2)Q_{33}}, \quad \varphi_1 = \frac{1}{Q_{13}+\kappa Q_{33}}, \quad \varphi_2 = \frac{1}{Q_{13}-\kappa Q_{33}}, \quad \varphi_3 = \frac{3Q_{33}+Q_{13}}{(9-\kappa^2)Q_{33}}, \quad \text{and } \kappa = \sqrt{\frac{Q_{11}}{Q_{33}}}. \tag{3.5}$$

To eliminate the constants, the displacement vector is written as:

$$\boldsymbol{u} = \boldsymbol{u_\omega} + \boldsymbol{\Phi_u C}. \tag{3.6}$$

The vectors $\boldsymbol{u}$, $\boldsymbol{u_\omega}$, $\boldsymbol{\Phi_u}$, and $\boldsymbol{C}$ from Equation 3.6 are defined as:

$$\boldsymbol{u} = \begin{pmatrix} u_{r_i} \\ u_{r_0} \end{pmatrix}, \quad \boldsymbol{u_\omega} = -\rho\omega^2\varphi_0 \begin{pmatrix} {r_i}^3 \\ {r_o}^3 \end{pmatrix}, \quad \boldsymbol{\Phi_u} = \begin{bmatrix} {r_i}^\kappa\varphi_1 & {r_i}^{-\kappa}\varphi_2 \\ {r_o}^\kappa\varphi_1 & {r_o}^{-\kappa}\varphi_2 \end{bmatrix}, \quad \text{and} \quad \boldsymbol{C} = \begin{pmatrix} C_1 \\ C_2 \end{pmatrix}, \tag{3.7}$$

where r_i represents the inner radius of the numerical ring and r_o represents the outer radius of the same numerical ring. Similarly, the stress vector from Equation 3.4 is written as a force vector:

$$\boldsymbol{f_b} = \boldsymbol{f_\omega} + \boldsymbol{\Phi_f C}, \tag{3.8}$$

where the $\boldsymbol{f_b}$, $\boldsymbol{f_\omega}$, *and* $\boldsymbol{\Phi_f}$ from Equation 3.8 are defined as:

$$\boldsymbol{f_b} = \begin{pmatrix} -r_i\sigma_{r_i} \\ r_o\sigma_{r_o} \end{pmatrix}, \quad \boldsymbol{f_\omega} = \begin{pmatrix} \rho\omega^2\varphi_3 {r_i}^3 \\ -\rho\omega^2\varphi_3 {r_o}^3 \end{pmatrix}, \quad \text{and } \boldsymbol{\Phi_f} = \begin{bmatrix} -r_i{}^{\kappa} & -r_i{}^{-\kappa} \\ r_o{}^{\kappa} & r_o{}^{-\kappa} \end{bmatrix}. \tag{3.9}$$

Stress-displacement relation for both the inner and outer surfaces of each numerical ring while also eliminating $\boldsymbol{C}$ is formulated using Equations 3.6 and 3.8. Stress-displacement relation is given as:

$$\boldsymbol{ku} = \boldsymbol{f_b} + \boldsymbol{ku_\omega} - \boldsymbol{f_\omega}, \tag{3.10}$$

where $\boldsymbol{k}$ is the stiffness matrix for the numerical ring is defined as:

$$\boldsymbol{k} = \boldsymbol{\Phi_f}{\boldsymbol{\Phi_u}}^{-1}. \tag{3.11}$$

Continuity conditions must be satisfied for adjacent rings which are given as:

$$\sigma_{r_0}^{(j-1)} = \sigma_{r_i}^{(j)} \quad \text{and } u_{r_0}^{(j-1)} = \sigma_{r_i}^{(j)}, \tag{3.12}$$

where j is used to denote the j^{th} numerical ring. Equation 3.10 satisfying Equation 3.12 is thus written globally as:

$$\boldsymbol{KU} = \boldsymbol{F_b} + \boldsymbol{F_\omega}, \tag{3.13}$$

where $\boldsymbol{K}$ is the global stiffness matrix and $\boldsymbol{U}$ is the global displacement vector which represents the displacement of each interface. The global force vectors, $\boldsymbol{F_b}$ and $\boldsymbol{F_\omega}$, is given as:

$$\boldsymbol{F_b} = \sum_{j=1}^{N} \boldsymbol{f_b^{(j)}} \quad \text{and } \boldsymbol{F_\omega} = \sum_{j=1}^{N} (\boldsymbol{k}^{(j)}\boldsymbol{u}_\omega^{(j)} - \boldsymbol{f}_{\boldsymbol{\omega}}^{(j)}), \tag{3.13}$$

where N is the total number of numerical layers in the flywheel. The evaluation of $\boldsymbol{F_b}$ results in a vector with mostly zeros as a result of the internal stresses. Sung K. Ha, et al, modeled an internal permanent magnet as an isotropic material which applies a pressure on the inner

surface. This resulted in a single non-zero term from this pressure in $\boldsymbol{F_b}$. The current low-speed flywheel built using iron laminations which in this thesis are modeled by inserting the isotropic properties into $\boldsymbol{Q}$ from Equation 3.1. This results in $\boldsymbol{F_b}$ being completely zero by removing the pressure applied to the inner surface.

The For each j^{th} ring, $\boldsymbol{k}$ is a (2 x 2) matrix. A global stiffness matrix, $\boldsymbol{K}$, results in a symmetric (N+1 x N+1) tridiagonal matrix found by:

$$\mathbf{K} = \begin{bmatrix} k_{11}^{(1)} & k_{12}^{(1)} & 0 & & 0 & 0 & 0 \\ k_{21}^{(1)} & k_{22}^{(1)} + k_{11}^{(2)} & k_{12}^{(2)} & \cdots & 0 & 0 & 0 \\ & k_{21}^{(2)} & k_{22}^{(2)} + k_{11}^{(3)} & & 0 & 0 & 0 \\ & \vdots & & \ddots & & \vdots & \\ 0 & 0 & 0 & & k_{22}^{(n-2)} + k_{11}^{(n-1)} & k_{12}^{(n-1)} & 0 \\ 0 & 0 & 0 & \cdots & k_{21}^{(n-1)} & k_{22}^{(n-1)} + k_{11}^{(n)} & k_{12}^{(n)} \\ 0 & 0 & 0 & & & k_{21}^{(n)} & k_{22}^{(n)} \end{bmatrix}. \quad 3.14$$

Similarly, the operation for $\boldsymbol{F_\omega}$ on each numerical ring $(\boldsymbol{k}^{(j)}\boldsymbol{u}_\omega^{(j)} - \boldsymbol{f}_{\boldsymbol{\omega}}^{(j)})$ results in a (N x 2) matrix and is summed together in the following manner to create a (N+1 x 1) vector:

$$\boldsymbol{F_\omega} = \begin{pmatrix} (\boldsymbol{k}^{(1)}\boldsymbol{u}_\omega^{(1)} - \boldsymbol{f}_{\boldsymbol{\omega}}^{(1)})_{11} \\ (\boldsymbol{k}^{(1)}\boldsymbol{u}_\omega^{(1)} - \boldsymbol{f}_{\boldsymbol{\omega}}^{(1)})_{12} + (\boldsymbol{k}^{(2)}\boldsymbol{u}_\omega^{(2)} - \boldsymbol{f}_{\boldsymbol{\omega}}^{(2)})_{21} \\ \vdots \\ \vdots \\ (\boldsymbol{k}^{(n-1)}\boldsymbol{u}_\omega^{(n-1)} - \boldsymbol{f}_{\boldsymbol{\omega}}^{(n-1)})_{(n-1)2} + (\boldsymbol{k}^{(n)}\boldsymbol{u}_\omega^{(n)} - \boldsymbol{f}_{\boldsymbol{\omega}}^{(n)})_{n1} \\ (\boldsymbol{k}^{(n)}\boldsymbol{u}_\omega^{(n)} - \boldsymbol{f}_{\boldsymbol{\omega}}^{(n)})_{n2} \end{pmatrix}. \quad 3.15$$

Solving the system of linear equations for $\boldsymbol{U}$ in Equation 3.13 in conjunction with Equation 3.2 allows for the $\boldsymbol{\varepsilon}$ vector be solved. Substituting $\boldsymbol{\varepsilon}$ into Equation 3.1 allows for the solving of $\boldsymbol{\sigma}$.

3.2 Model Validation

The model is first developed to have two physical rings. Multiple other physical rings can be added with the addition of the other properties. The top and bottom stainless caps are being excluded from this preliminary model because the machined geometry will require a finite element model. Once a rotor size and design is selected, the addition of caps can be added to the model or will give a sensible starting point for the finalization of the cap material and geometry. In order to validate the model, an initial study is conducted where the two physical rings are made to be the same isotropic material which is chosen to be the M-36 silicon-iron currently being in use. The model sees that setting the physical rings to be the same material is the equivalent to one physical isotropic ring. Comparison of between the model and the isotropic equations can now take place. Physical properties for M-36 steel are given in Table 3.1 [31].

Properties	Value
Young's Modulus (E)	200 (GPa)
Poisson's Ratio (ν)	0.29
Density (ρ)	7700 (kg/m^3)
Yield Stress (S_y)	290 (MPa)

Table 3.1: Physical properties for M-36 laminations [31]

The analytical stress and displacement equations for an isotropic stress state of a hollow flywheel with a constant thickness at a specific rotational velocity are given below [24]:

$$\sigma_r = \frac{3+\nu}{8}\rho\omega^2\left[a^2 + b^2 - r^2 - \frac{a^2b^2}{r^2}\right]$$

$$\sigma_\theta = \frac{3+\nu}{8}\rho\omega^2\left[a^2 + b^2 - \frac{1+3\nu}{3+\nu}r^2 + \frac{a^2b^2}{r^2}\right] \quad 3.16$$

$$u_r = \frac{3+\nu}{8}\rho\omega^2\frac{1-\nu}{E}r\left[a^2 + b^2 - \frac{1+\nu}{3+\nu}r^2 + \frac{1+\nu}{1-\nu}\frac{a^2b^2}{r^2}\right] \quad 3.17$$

where *a* and *b* are the inner and outer radii respectively, *r* is a continuous variable for the radial distance from *a* to *b*, and the other properties are given in Table 3.1. Equations 3.16 and 3.17 are developed under the plain stress assumption thus $\sigma_z = 0$ and is not considered in this comparison. An angular velocity ω = 10,000 rpm will be used for initial validation. Any angular velocity can be used as a result of the yield stress of the material not affecting the stresses and displacement outputs from the models. An inner radius of r = 0.0762 meters (3 inches) and an outer radius of r = 0.1778 meters (7 inches). The inner radius is an approximately the current radius of the UIFESS. The outer radius was arbitrarily selected such that the composite can be inputted for comparison. Comparison of the radial stress is done by plotting σ_r from Equation 3.1 and Equation 3.16 as shown in Figure 3.4. Likewise, the hoop stress is compared by plotting σ_θ from Equation 3.1 and Equation 3.16 as shown in Figure 3.5. The plain strain assumption for the model and plain stress for the isotropic equaitons do not allow for comparrison of the stress in the z-directon.

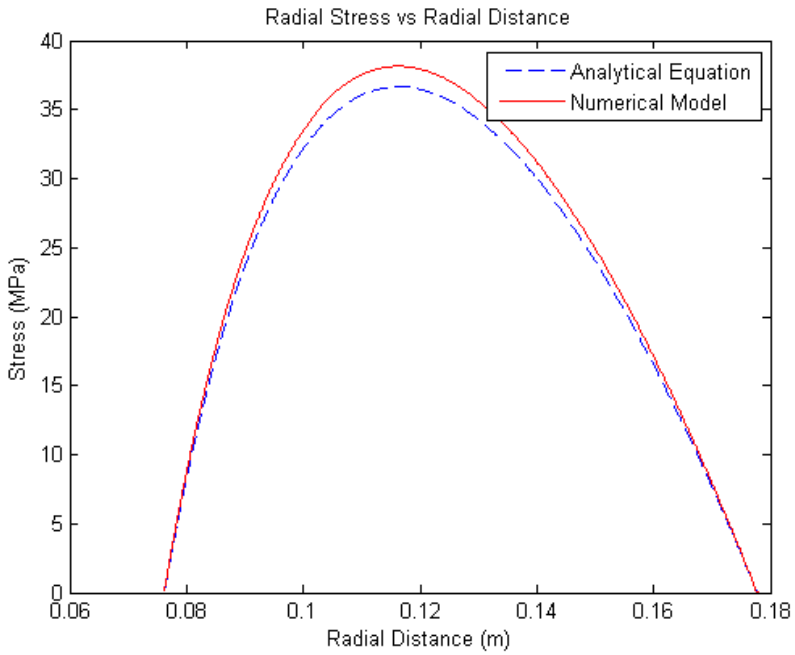

Figure 3.4: Comparison of radial stress (MPa) vs radial distance (m) for the numerical equation and the analytical model at ω = 10,000 rpm

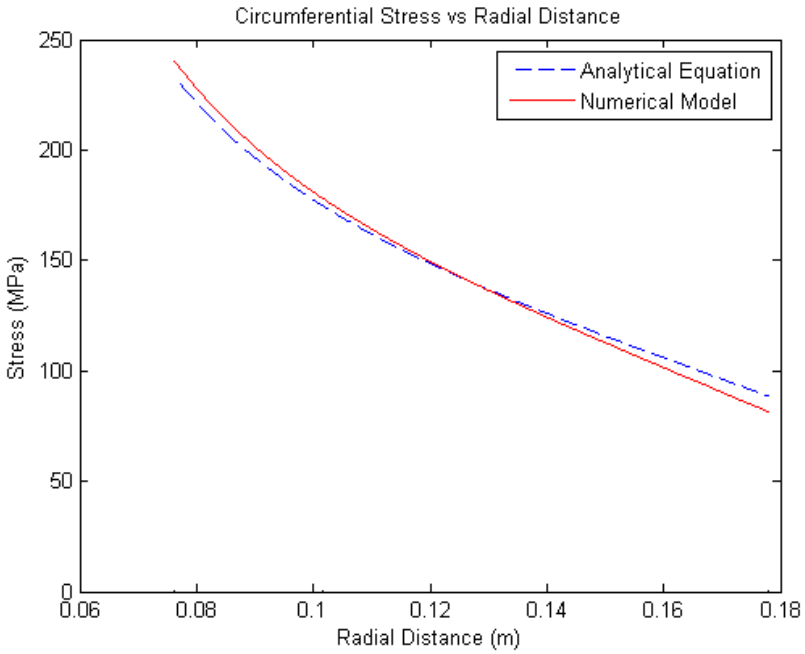

Figure 3.5 Comparison of hoop stress (MPa) vs radial distance (m) for the numerical equation and the analytical model at ω = 10,000 rpm

For the radial stress in Figure 3.4, the model predicts a stress that is about 5% greater than the radial stress from Equation 3.16 along the entire radius. A 5% error at a larger stress near the middle results in a greater magnitude of a stress difference. When using fewer numerical rings (<50), the model predicts the radial stress with an error that is approximately 5% greater than Equation 3.16. Using many number numerical rings (>1500) marginally decreases this error to about 4%. The hoop stress, which is the highest stress, shows an error that is approximately 3% high at the inner radius and approximately 8.7% low at the outer surface. The number of numerical rings had a no influence on the changing of these values.

While the model does not match the isotropic equations exactly, the errors are relatively small. Both the model and the isotropic equations are not exact as they were derived from a linear-elastic, mechanics of materials approach rather than a continuum approach. The mechanics of materials approach results in approximate values and not exact values. Some assumptions include small-displacements, line-elastic behavior, homogenous and uniform properties throughout. It is shown in the comparison that the model is more conservative by predicting higher stresses at the inner surface will allows for the continued use of the model. Lower yield strength for the iron laminations makes it the critical component with highest stress being at the inner-most surface.

The stress output is important from a stance of mechanical failure; however, the displacement is critical for electrical control. The strength of the forces applied from the stator are greater the smaller the airgap between the stator and the rotor [14]. The model will confirm whether or not previously determined 1 mm airgap can be maintained given the design and rotational velocity. In Figure 3.6 the differences between the displacements of the model and Equation 3.17 is shown.

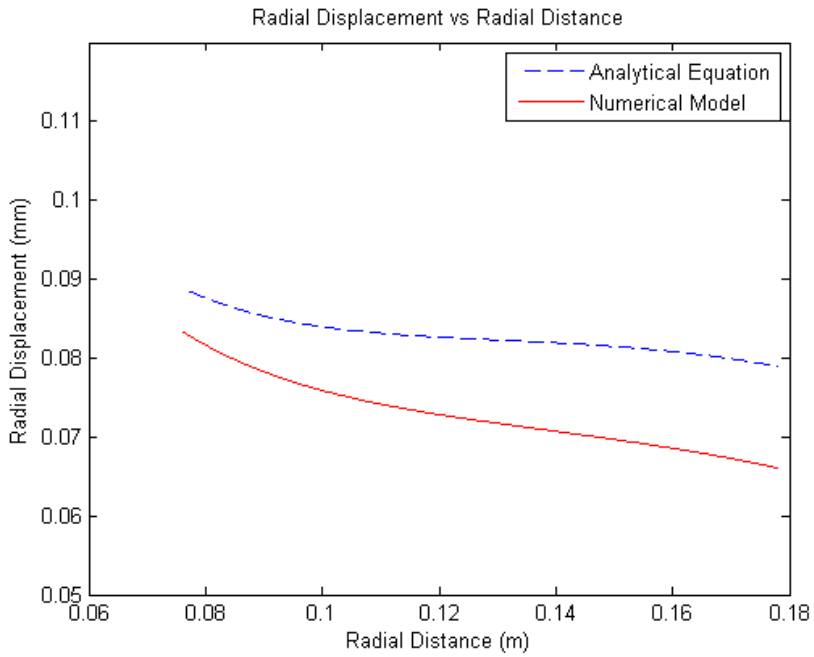

Figure 3.6: Comparison of radial displacement vs radial distance for the numerical equation and the analytical model at ω = 10,000 rpm

The model outputs a displacement that is approximately 6.2% low on the critical inner surface and approximately 16.2% low on the outer surface. The number of numerical rings and the change in angular velocity had negligible effects to these differences. A lower displacement from the model than the isotropic equations is therefore under-conservative. The large error is a result of the numerical model being derived in plane strain and Equation 3.17 being derived in plane stress. A vertical stress results in a subtraction of radial strain due to Poisson's effects. Including the displacement from Poisson's strain, that is previously subtracted, results in a more accurate prediction of the displacement. When this extra strain is added, the error range is similar to that of the hoop stress. This concludes that the effect of the strain induced by Poisson's ratio from the stress in the vertical direction from the plane strain assumption is the reason for the high error. This may be a way to adjust the model for a multi material design.

3.3 Model Adjustments

Two physical rings where originally introduced into the model for simplicity of verification. Additional rings can and will be added later. Adjusting the stiffness matrix $\boldsymbol{Q}$ allows for an axisymmetric composite ring to be incorporated into the model. Carbon fiber was chosen as the initial input for the ring for its ability to withstand high stresses. HexTow® HM63 with HexPly® 8552 Resin System, with properties found in Table 3.2, has a reasonably high yield stress while still having a modulus of elasticity greater than the iron laminations [32]. It is beneficial that the material stiffness's increase for each physical ring as radial distance increases. This gives additional insurance that separation of subsequent rings will not occur and additional support of the stresses from the inner ring. Other methods of reducing the chance of separation include pre-stressing during manufacturing and press-fitting the inner rings into subsequent rings. High modulus carbon fiber has a specific strength that is approximately 32 times greater than the M-36 iron laminates. The low density reduces the centrifugal forces by decreasing the mass while the higher modulus carries some of stress from the iron laminations. The three stresses for the solid iron flywheel as described previously are shown in Figure 3.7. The stress results of having an iron-carbon fiber rotor design are shown in Figure 3.8.

Lamina Properties	Value
Tensile Modulus (E_θ)	246 (GPa)
Transverse Modulus (E_r/E_z)	7.5 (GPa)
In-plane Poisson's Ratio* ($\nu_{\theta z}/\nu_{\theta r}$)	0.25
(r-z plane) Poisson's Ratio* ($\nu_{\theta z}/\nu_{\theta r}$)	0.2
Density (ρ)	1618 (kg/m^3)

Table 3.2: Physical properties for HM63 carbon fiber at 60% volume fraction. *Approximate value [32]

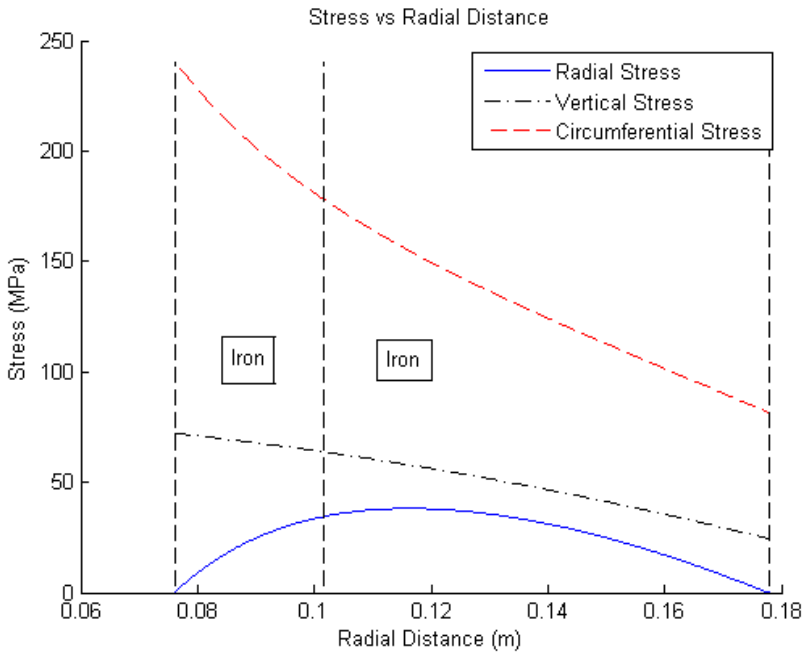

Figure 3.7: Radial, vertical, and circumferential stresses for iron-iron arrangement at ω = 10K rpm

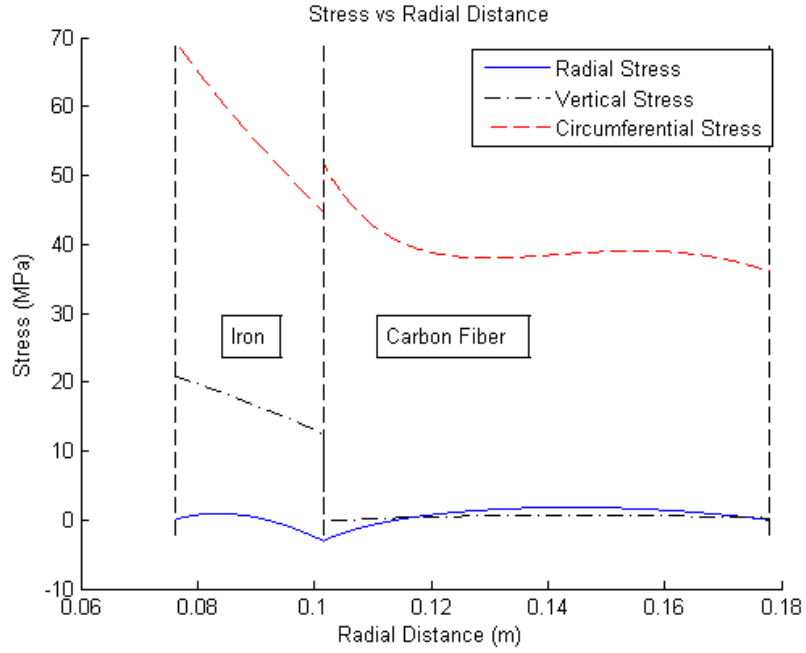

Figure 3.8: Radial, vertical, and circumferential stresses for iron-carbon fiber flywheel at ω = 10K rpm

The stresses in Figure 3.8 are reduced when the composite ring is added. Lower stresses indicate the possibility of adjusting dimensional parameters and rotational velocity in exchange for the deduction of stress to prevent failure while still maintaining high energy

storage. While the circumferential and vertical stresses are discontinuous, the radial stress is continuous which is required for the displacement, as shown in Figure 3.9, to be continuous throughout the flywheel. The confidence in the accuracy of the displacement is low; however, it does give an order of magnitude estimate for what the displacement will be. High displacement towards the outside surface in Figure 3.9 is a result of the low transverse modulus for the carbon fiber. Displacement of the outer surface does not affect the FRRM but may induce limitations for position sensors.

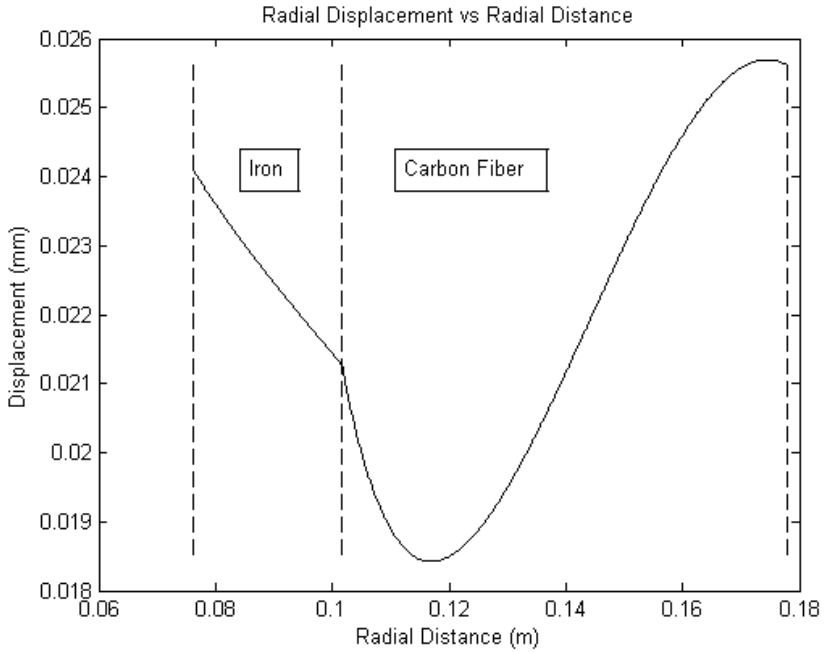

Figure 3.9: Radial displacement for iron-carbon fiber arrangement at ω = 10K rpm

A large displacement at the inner radius is detrimental for the control of the flywheel. Increasing the strength of the lamination and composite material will reduce the displacement. The extent that the stiffness would need to increase is beyond a feasible bound for materials. An increase in stiffness will likewise increase the stress in the flywheel which is already experiencing failure at speeds greater than 20,000 rpm. A reduction in the size of

the rotor will also decrease the stresses and displacements. A flywheel size required to not experience excessive displacements is much smaller than the stator can be built.

Large displacements will therefore require a much lower angular velocity or a way to "capture" the flywheel to maintain the 1 mm airgap necessary for control. One proposed method is to taper the inside surface and stator. When radial expansion occurs the superconducting plate can be actuated vertically. Actuation of the plate will result in an actuation of the flywheel itself therefore maintaining the required airgap. Currently for the UIFESS, the iron laminations are held in place using bolts that extend vertically through the flywheel. Theses laminations will still need to be held together for the high-speed FESS. Laminations of different diameters may not allow bolts to pass through the laminations. Bolts will likewise induce stress concentrations and shearing. A proposed method is a stainless steel sleeve implemented between the iron and composite such that the caps can then be attached to this sleeve. To achieve the inside taper, the iron laminations will need to be separate discrete diameters. These discrete diameters will create a surface that is no longer smooth but step-like. Typical properties of 304 Stainless Steel are given in Table 3.3.

Properties	Value
Young's Modulus (E)	193 (GPa)
Poisson's Ratio (ν)	0.29
Density (ρ)	8000 (kg/m^3)
Yield Stress (S_y)	290 (MPa)

Table 3.3: Physical properties for 304 Stainless Steel

A geometrically non-uniform rotor induces the complication of non-uniform deformation. This results in the inner tapered surface no longer being linear but arced. If the extent of this arc is too great, the shape of the flywheel will no longer match the taper of stator. Non-uniformity between the rotor and stator will result in unequal applied forces to the rotor from the airgap no longer being uniform. To decrease the uniformity, an angle can

be added between iron-stainless steel interface and another between the stainless steel-carbon fiber interface as shown in Figure 3.10 below.

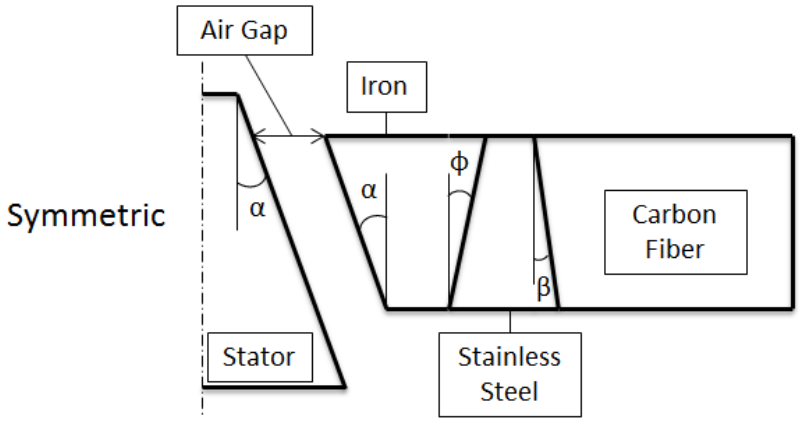

Figure 3.10: Schematic of the rotor's cross-sectional view

The taper angle α, iron-stainless steel angle ϕ, and the stainless steel-carbon fiber interface β are shown in Figure 3.10. The variables α, ϕ, and β, as shown in Figure 3.10, are defined as the positive direction. Given a value of α, ϕ and β can be adjusted such that the variation in radial displacement of the internal surface is minimized. Description of a heuristic approach to minimizing the deflections is described in Chapter 4. Similarly, a heuristic method of maximizing the rotational kinetic energy such that the maximum stress in the iron laminations does not exceed the yield stress is described in Chapter 4. For the maximizing optimization, it is assumed that $\alpha = \phi = \beta = 0$ as defined in Figure 3.10.

Chapter 4. Optimization

4.1 Introduction

Often times in design, the best set of design variables is not a trivial solution. To resolve this issue, a rigorous method of locating the optimum set of design variables is needed. Optimization methods are a systematic way of finding the optimal design. Using the parameters, an optimization can be formed into Standard Optimum Form. This form is the basis of all optimization algorithms.

The Standard Optimum Form is the minimization of a cost function, also known as the objective function, subject to constraints [33]. The cost function, *f(x),* is the value that is trying to be minimized. Constraints on the cost function can be equality, *h(x),* or inequality, *g(x),* constraints. Optimization functions are formulated to minimize a value, therefore, to maximize a value the cost function becomes *–f(x).* An example of the cost function and constraints are given below:

- Cost function: "Minimize the cost of a wing given a set of design parameters."
- Equality constraint: "A wing must be 10 feet long."
- Inequality constraint: "The wing must weigh less than 100 lbs."

Given an arbitrary set of design variables $\mathbf{x} = [x_1, x_2, \ldots, x_n]$, the Standard Optimum Form for a function and constraints is shown in Equation 4.1. For any given design problem there may be both, either or neither equality and inequality constraints [33].

Minimize:

$$f(\boldsymbol{x}) = f(x_1, x_2, \dots, x_n)$$

subject to the equality constraints:

$$h(\boldsymbol{x}) = h(x_1, x_2, \dots, x_n) \quad 4.1$$

subject to the inequality constraints:

$$g(\boldsymbol{x}) = g(x_1, x_2, \dots, x_n).$$

Design variables in an optimization can be either continuous or discrete. Continuous variables are ones that can vary by any value within the bounds prescribed. An example of a continuous variable is the length of a member used in the construction of a table. Discrete variables are ones that are limited by specific set of standard values. Examples of these are standard pipe sizes or board thicknesses.

Constraints are introduced the through the use of the Lagrange Multiplier Theorem as given in Equation 4.2 [33].

$$\boldsymbol{L} = f(\boldsymbol{x}) + \sum_{i=1}^{p} v_i h_i(\boldsymbol{x}) + \sum_{j=1}^{m} u_j g_j(\boldsymbol{x}), \quad 4.2$$

where $\boldsymbol{L}$ is the Lagrangian Function and v_i and u_j are the Lagrange multipliers for the equality and inequality constraints respectively. The number of equality and inequality constraints are defined by p and m respectively. Lagrange multipliers are implemented for the use of minimizing the error added from the constraints. Using the Lagrange multipliers in the Largrangian Function allows the function to be solved as an unconstrained function. At a feasible, optimal point $\frac{\partial \boldsymbol{L}}{\partial \boldsymbol{v}} = \frac{\partial \boldsymbol{L}}{\partial \boldsymbol{u}} = \boldsymbol{0}$ [33].

Much like in calculus, a design function can have multiple minima and maxima as shown in Figure 4.1 [33]. In most cases, there is no way to know for certain if the optimum found is the global optimum. One way to find the global optimum is the use of graphical

optimization. This is done by plotting the function or function contour plains and constraints to find the optimum value. For instance, a global minimum at point *E* and a global maximum at *F* are shown in Figure 4.1. Points *B* and *D* are local minima while *A* and *C* are local maxima. This type of optimization is limited to the number of design variables that can be plotted. This requires the use of algorithms to find the optimal solution.

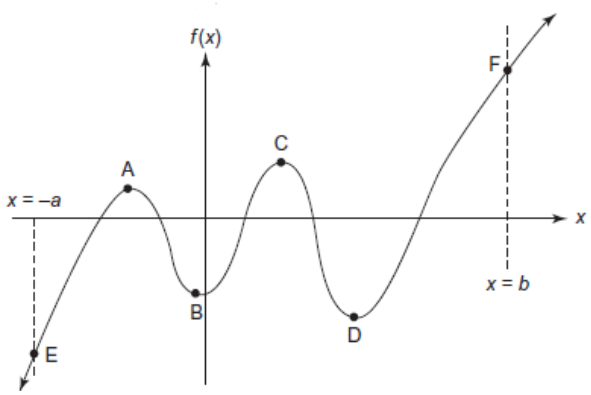

Figure 4.1: Representation of local and global minima and maxima [33]

Two divisions of optimization algorithms exist; gradient and heuristic. Incorporating the model into an optimization method must be done by the use of heuristic optimization methods. Gradient based optimizations incorporate the use of derivatives to search for an optimum location. These require having a continuous function or enough information for numerical differentiation. Heuristic optimizations initiate several starting points and use search algorithms to locate the optimum. Gradient based and heuristic optimizations have potential to be significantly influenced by the starting location. This can be influenced by the optimization method or how the design variables affect the objective function. For heuristic optimizations, it is best to have widespread coverage of the design space. Widespread coverage helps to insure locations of the design aren't misrepresented. This will be done through the use of Latin Hypercube Sampling (LHS).

4.2 Latin Hypercube Sampling

One method of population initiation is complete, random sampling. Selecting randomly risks the chance of points clustering in certain regions resulting in a poor distribution of the design space. Clustering is likely for when low population sizes are prevalent. This can be remedied with the use of LHS. Sampling LHS is used to guarantee widespread initiation in the design space [34].

To select a population, the design space is evenly gridded into bins such that the number of bins is the same as the pre-selected population. The size of the population needed is problem to problem dependent but often correlates roughly to the number of design variables. The more design variables, the larger the population size will need to be. Once the design space is gridded points within that grid need to be selected. This is done by randomly selecting a permutation of the variables which represents a grid location. For a simple 2D case, if a grid location of an (x,y) location is selected, no other data points can be selected in column of x nor the rows y occupied by that point. Figure 4.2 demonstrates the use of LHS to select five points in 5X5 grid. LHS results in each row and column containing a data point. This point is typically located at the midpoint of the grid however some extra randomness is built into LHS routine by adding a random number to the midpoint to shift it throughout the grid region. Using the same process, this can be applied to multiple dimensions to form a hypercube.

5				4	
4					5
3		1			
2	2				
1			3		
Y/X	1	2	3	4	5

Figure 4.2: LHS example for two variables and 5x5 grid [34]

4.3 Particle Swarm Optimization

The model developed in Chapter 3 analyzes the stress state and radial displacement of the flywheel. Model outputs are needed for the optimization therefore each point in the optimization function will need to be inserted into the model. Unless enough points are input into the model to form a surrogate model, gradient based optimization methods cannot be used. This consequently introduces the need for a heuristic approach which does not require a continuous function. Heuristic methods use searching algorithms rather than gradient based searching methods. Searching algorithms use the objective function evaluations to determine the searching direction. Gradient based methods, however, use both the objective function evaluations and the derivatives to determine the search direction [33]. An example of a heuristic optimization approach is Particle Swarm Optimization (PSO). Particle Swarm Optimization was selected for its wide range of applicability and implementation simplicity. The described optimizations in Sections 4.4 and 4.5 incorporate the use of continuous design variables which PSO's are well suited for.

PSO was developed in 1995 by James Kennedy and Russell Eberhart with methodologies comprised from bird flocking to food and evolutionary computing [35]. Each particle that is initiated represents a bird in a flock trying to find a food source. Each bird communicates to determine which of its surrounding neighbors is nearest a food source. The bird then moves in that direction. This is analogous to particles moving toward other particles that have the lowest value. If the bird realizes that the best location is on a previous iteration, it tends to move towards the best location. In PSO, the best point for each particle is stored. At each iteration, a comparison is done between a particle's best location and its

current location. This is referred to as the fitness function because it determines how the quality of its location with that in its stored history.

While a particle moves it compares the neighbors and its own fitness function to determine the final direction of movement. The number of neighbors being considered is ~25% of the population number. Having a reasonably small number of neighbors will help insure that large jumps aren't made through the design space. As a bird is flying to a source, it may realize that the better location is behind it. Already traveling in that direction, the bird will want to continue in that approximate direction and resist going in the opposite direction. This is similar to momentum of an object and is accounted for in the PSO by what is referred to as a velocity term. This is not a true velocity but a measure of how quickly the particle is moving through the design space. Kennedy's and Eberhart's PSO algorithm is given in Equation 4.3:

$$vx(k+1) = vx(k) + rand * p_{increment} * \big(pbestx(k) - presentx(k)\big), \qquad 4.3$$

where *vx* is the velocity for the particle and *k* is the iteration number. *Rand* is a random number between zero and one and used to induce randomness in the system such that more coverage of the design space occurs. A modifying factor $p_{increment}$ is used to weight the fitness function determining how far it will move in the direction of the particle's history best . The group's best point, *pbestx*, is the global best point. This includes each particle and all iterations. Variable *presentx* is particle's current position. Since the development of Equation 4.3, it has been modified to incorporate added flexibility and efficiency as given in Equation 4.4 [36]:

$$v_{id} = w * v_{id} + c_1 * rand * (p_{id} - x_{id}) + c_2 * Rand * (p_{gd} - x_{id}), \quad 4.4$$

where v_{id} is the velocity term and w is the inertial weight similar to inertia. Constants c_1 and c_2 are greater than one and used to weigh a particle's best position and its best neighbor. *Rand* and *rand* are random numbers between zero and one used to improve widespread, sporadic search of the design space. A particle's best point, p_{id}, used as part of the fitness function while p_{gd} is the best neighbor's location. The current location of the particle is represented by x_{id}. Equation 4.4 was shown by Eberhart and Shi to be more efficient compared to Equation 4.3. The inertial weight w is a number that is either less than one or initially one and updated at each iteration by a factor less than one. It can be adjusted on subsequent iterations such that the particles essentially slow down at a desired rate. This increases the rate at which the points converge. Having an inertial weight w too small increases convergence but decreases the ability of the particles to search the design space. Each particle's location is then updated using Equation 4.3 in conjunction with Equation 4.2:

$$x_{id} = x_{id} + v_{id}. \quad 4.5$$

The objective function is what the PSO function is trying to minimize. This objective function value is the evaluation of the particle locations and can be written as shown in Equation 4.3 [33]. A lack of a continuous function requires that Lagrange multipliers be introduced as an incrementally increasing penalty value.

$$f(\boldsymbol{x}) = f(\boldsymbol{x}) + Penval * g, \quad 4.6$$

where $f(\boldsymbol{x})$ is the function evaluation, *Penval* is a scaling factor, and g is the constraint of the penalty function. The penalty function is the evaluation of constraints that are added to function that keep the particles from moving into an infeasible region or completely out of the design space.

Frequently, the optimum set of design variables is located near a boundary of one or multiple constraints. If a particle is violating a constraint near a boundary, the magnitude of the violation error is comparatively small. This may result in the optimization function giving less precedence to the boundary condition. Incrementally increasing *Penval* as the point converges gives appropriate significance to the constraint.

4.4 Displacement Optimization

As previously stated and shown in Figure 3.10, a way of maintaining a 1 mm airgap is to taper the rotor and flywheel then actuate the rotor vertically. The forces from the bearing are inversely proportional to the gap distance [14]. A small increase in the airgap distance significantly reduces the applied force to the flywheel. In an effort to control for uniform displacement for a given value of α, a PSO was tailored to minimize the variance in displacement in the vertical direction for the inner surface. Incorporation of the angles α, ϕ, and β is done by separating rotor's thickness into multiple discrete layers. These discrete layers are given separate radii then the adjacent layers. Using discrete radii allows the values of the tapers to be included into the model. The current radial lamination thickness is set to be the minimum thickness of the iron which is 0.02776 meters. If stainless steel or a similar material is used to hold the laminations and caps together, the probable assembly will require bolts to connect the sleeve and caps together. For this reason, the minimum thickness of the stainless steel is set at 13 mm to allow for the connection. The smallest inner radius, at the top, is set to 0.0762 meters which is the approximate inner radius for the UIFESS. The outer radius is set at 0.1778 meters which is estimated based on the size UIFESS. The total height in the model is h = 0.2286 meters.

The design variables for the displacement PSO are $x_1 = \phi$ and $x_2 = \beta$ where $\boldsymbol{x} = [x_1\ x_2]$. The side bounds for this PSO are [-5° 10°] and ±5° for ϕ and β respectively. From Equation 4.4, f is the maxim variation in displacement and g is the squared sum of the violation of the side bound constraints. Population initiation is done by the use of LHS. A depiction of a population initiation is shown in Figure 4.3.

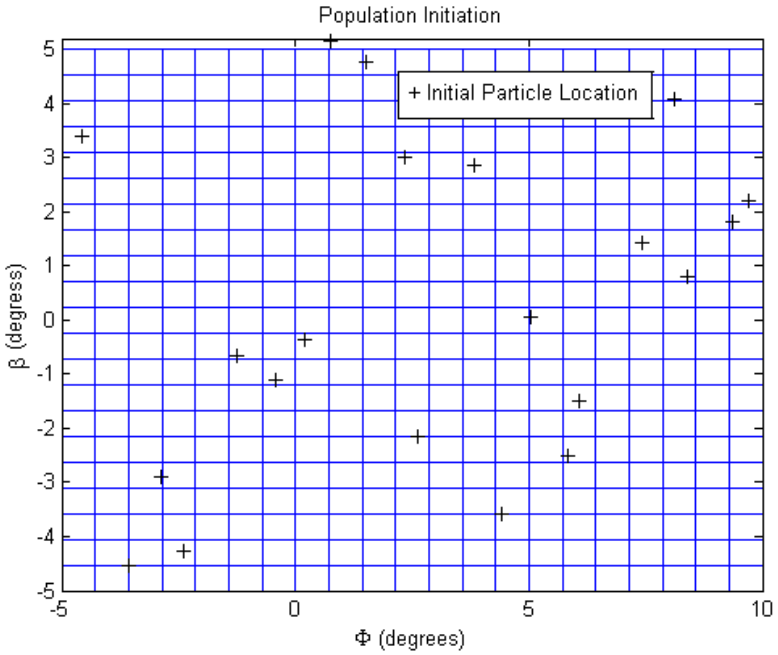

Figure 4.3: Population initiation using LHS for the displacement PSO

The use of LHS resulted in a reasonable coverage of the design space. The population size for the two design variables is selected as 21 particles. Using six neighbors, the particles have the ability to converge to different optimum values. Twenty-one particles are used because the low number of design variables and the significant length of time to evaluate the model. Values used in the PSO such as those for Equations 4.2 and 4.4 are given in Table 4.1. The variables containing *initial* are set for the first iteration value and are updated by a factor using those containing *update*. The exception to this is $v_{id\_initial}$ which is updated using Equation 4.2.

Variable	Value
Population	21
# Neighbors	6
c_1	1.2
c_2	1.2
$w_{initial}$	1
w_{update}	0.75
$Penval_{initial}$	0.1
$Penval_{update}$	2.0
$v_{id\_initial}$	0.4
ω (rpm)	50K

Table 4.1: Variable values needed for displacement PSO

An exit criterion, also known as convergence criterion, is needed to determine if the PSO has located an optimum location. Many options for convergence exist; however, in the case of the displacement optimization the convergence criterion is defined as the all the particles stop moving. Essentially, the distance between the particles' location of the current iteration and the previous iteration must below a critical value ε. The range of the design variables are small thus ε = 0.1 is a sufficiently tight tolerance for convergence.

This PSO converges to the given criterion in 90 iterations and approximately 1.75 hours. The large length of time is a result of multiple discrete layers in the model. Given the size and parameters, the optimal values are ϕ = 6.03° and β = 2.65°. These angles result in an overall difference in displacement of 0.11 mm. Given dramatically different values for β resulted in similar results. This concludes that the displacement is much more sensitive to α than β. More shallow angles for β is more beneficial for manufacturing. The PSO model converges to same general location every time. The first, middle, and last iterations are shown in Figure 4.4. The relative shape of the flywheel with the optimized angles is shown in Figure 4.5, not to scale. Without the use of the optimization, using $\phi = \beta = 0$ and $\alpha = 5$, the difference of the inner displacement would be approximately twice as large. Similar values of ϕ and β where found at ω = 20,000 rpm.

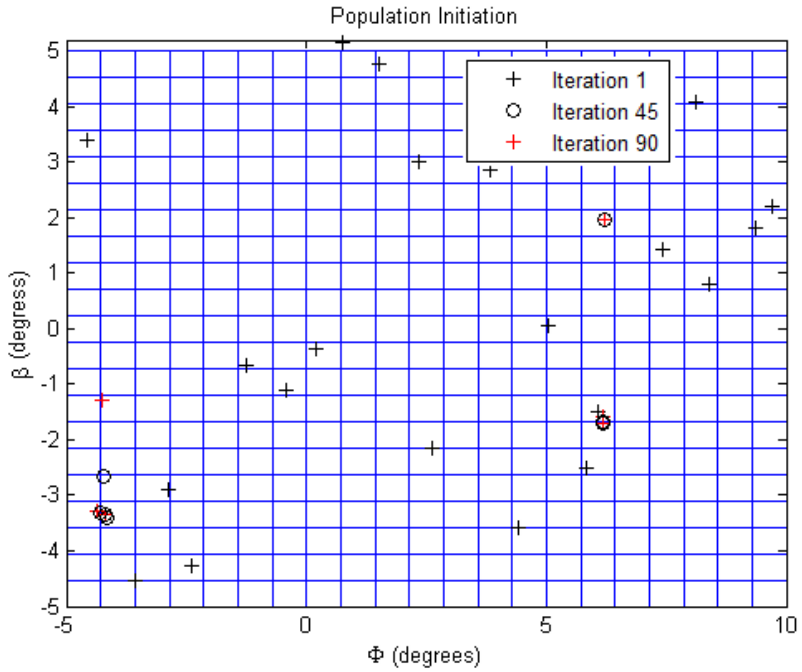

Figure 4.4: Particle convergence locations at different iterations

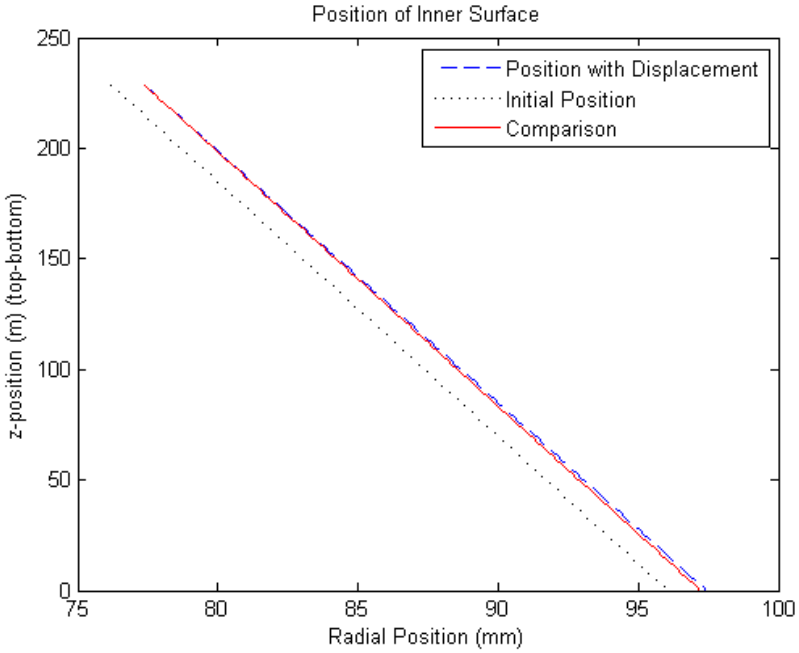

Figure 4.5: Geometrical comparison after deformation at 50k rpm (not to scale)

4.5 Energy Optimization

The goal of the high-speed UIFESS is to safely store large quantities of energy while structural integrity. The weakest portion of the rotor is the iron laminations with a yield stress of Sy = 290 MPa. The same material layup as Figure 3.10 is used however $\alpha = \phi = \beta = 0$. Two separate energy PSO functions are used to maximize the stored energy. One uses four independent variables which are the radiuses to the surfaces as shown in Figure 4.6 given an angular velocity. The second uses the same variables as the first with the inclusion of the angular velocity as a design variable. A fixed angular velocity will show the relation between angular velocity and the maximum kinetic energy. Optimization algorithms are formulated for the minimization of a value. In order to maximize a value, the minimization of the negative is used therefore Equation 4.4 becomes [33]:

$$f = -f + Penval * g. \tag{4.5}$$

The function value of $-f$ is the negative of the kinetic energy of the rotor. The constraint values are still positive making f larger and therefore a worse location according to the PSO algorithm.

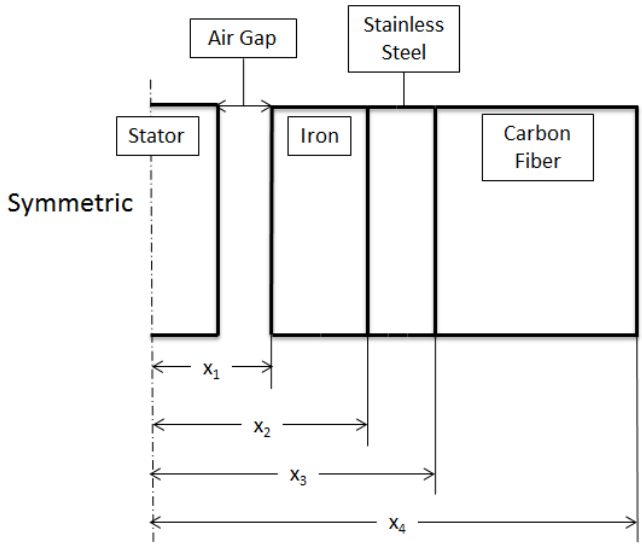

Figure 4.6: Independent design variable inputs for energy optimization

Each material ring is given a minimum and maximum value for the radial thickness. Initiation for both the four and five variable PSO functions is done using LHS. Multiple dimensions eliminate the possibility of giving a physical representation of the population scatter. For the 2D PSO with a well-defined design space, only 21 particles are needed. The design space for the four and five variable is a function of the thickness of the material layers making it less defined. Adding a constraint that hoop stress in the iron must be less than the yield stress creates a feasible region of the design space that is immensely uncharacterized. For this reason, 125 particles are used for the 4D PSO and 151 particles for the 5D PSO. At higher velocities, the feasible region is much smaller and more difficult to find. To remedy this, 201 particles are used to increase the likelihood of a point starting in a feasible region at velocities greater than 30,000 rpm. Other parameters used in the optimization are given in Table 4.2. Subjecting the PSO to the yield constraint forces the PSO from making the flywheel very large and very fast. To increase the rate of convergence, the best, feasible particle is seeded at each iteration.

Variable	Value
Population	125/151
# Neighbors	50
c_1	1.2
c_2	1.2
$w_{initial}$	1
w_{update}	0.95
$Penval_{initial}$	10
$Penval_{update}$	1.5
$v_{id\_initial}$	1.0

Table 4.2: Variable values needed for energy PSO

Implementing the design variables into the model requires that they be in meters for x_1, x_2, x_3, and x_4 and for the 5D case x_5 is in rpm. The model outputs the stress in MPa. Large orders of magnitude between the dimensional inputs, stress, and rpm require scaling the

values. Without scaling, variables will be misrepresented. The dimensional values are scaled such that x_1, x_2, x_3, and x_4 range from zero to one. The stress is scaled by the yield stress, and the angular velocity, ω, is scaled to range from one to ten with actual values ranging from 10,000 rpm to 100,000 rpm. Scaling the kinetic energy by 10^{-4} allows for proper representation of the penalty and constraints on the objective function value. Having too large a penalty at the first several iterations will force the particles in the PSO to move too far imposing the possibility of moving past the feasible design region.

At a higher angular velocity, the flywheel will need to be smaller to satisfy the stress constraint. Thus there is a tradeoff in the Equation 1.1 between a large moment of inertia, *I*, and the angular velocity ω. Evaluating the 4D PSO in 5K rpm increments results in the comparison of the stored energy and the angular velocity. This is shown in Figure 4.7.

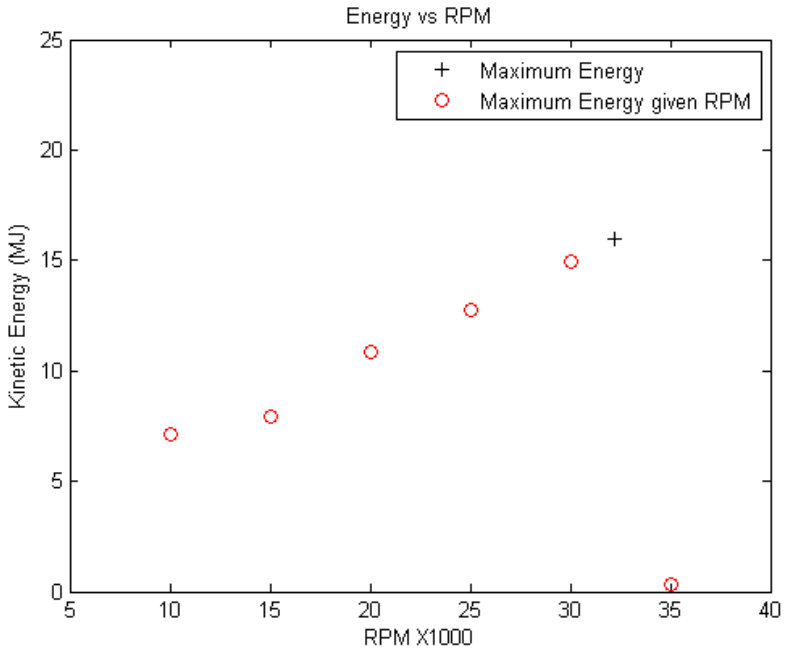

Figure 4.7: Comparison of the maximum energy and RPM

Energy storage at 35K rpm is much smaller as a result the decrease in the rotor's size. Beyond this point the optimization function is not able to locate a feasible point. The optimum radial values for the maximum energy storage is **x** = [0.0394 0.0544 0.0608 0.2631] meters at an angular velocity of approximately 32,200 rpm. The stored kinetic energy for this size and angular velocity is ≈16 MJ. This is equivalent to ≈3.8 kg of TNT. Given the size and density of the materials, the mass is found to be 88 kg. Lower speeds, such as 10,000 rpm, resulted in even large flywheel with a mass 239 kg and dimensions of **x** = [0.0991, 0.1476, 0.1726, 0.3731] meters. At large thicknesses of carbon fiber, some of the load is carried from the laminations. Beyond this point, added material increases the energy greatly while slowly increasing the stress.

At ω = 25,000 rpm the optimization converged to **x =** [0.050, 0.071, 0.079, 0.282] meters with a resulting energy of 12.76 MJ and a mass of 105 kg. This flywheel is still very large compared to the optimal value at 32,200 rpm. The inner radius is still smaller than the current UIFESS however it is larger than the optimal values found at and above 30,000 rpm. Having a larger inside radius allows for more room for the wires when the new stator will be wound. For 25,000 rpm design, the radial displacement of the inner surface is 0.11 mm. This displacement isn't enough to require a tapering of the flywheel which would increase the complexity of the system. If a lower modulus material were to be used, it could be possible that the surface displacement be large enough to require a taper.

Chapter 5. Summary, Future Work, and Conclusions

5.1 Summary

The University of Idaho is developing a flywheel energy storage system. The low-speed UIFESS has been designed and a built but not fully completed. The completion and testing of the UIFESS will produce a foundation for which the high-speed FESS can be built upon as part of the Steckler Phase III portion of the project. This thesis presents the development of a numerical model that aids in design of the high-speed flywheel.

At high rotational speeds, the induced stresses from the centrifugal forces become a limiting factor in the design of the flywheel. This model calculates the stress while incorporating the use of both isotropic and anisotropic materials. Isotropic iron laminations are needed for the FRRM. This machine is responsible for both the power input and power output of the FESS. Use of composite materials increases the specific energy of the system by linearly increasing the mass but exponentially increasing the energy through an increase in size and rotational velocity. The composite materials are assumed to be orthotropic continuous fiber composite. The addition of multiple rings into the model is possible if needed for further construction or a deduction in stress discontinuities. Comparison of the model with analytical equations revealed that the stress is calculated within reasonable bounds while the displacement varies as a result of the differences in developmental assumptions.

In addition to the development of the numerical model, two separate optimization functions were developed. One is to minimize the variation in displacement for a tapered inner surface and the other is to maximize the kinetic energy of the rotor. Using outputs from the model requires that the optimization method be a heuristic method. Particle Swarm

Optimization is the selected method. Heuristic methods are used in the absence of the possibility for taking the derivative of a function either symbolically or numerically. Heuristic optimization methods use a searching algorithm to find minimum locations. Wide range of applicability exists with these methods. With application, there is however a sacrifice in computation time. Gradient based methods typically produce results in seconds to a few minutes where PSO can take up several minutes to hours to converge to a set of design variables.

Minimization of the change in displacement is significant if a taper is required for the flywheel. A tapered surface will be needed if airgap cannot be maintained within reasonable bounds at high rotational speeds. The introduction of such a surface will produce non-uniform displacement. Minimal change in displacement will insure that more uniform forces can be applied to the rotor. Maximizing the kinetic energy in the rotor is a goal of the project. This optimization will bound the both the rotor size and the maximum angular velocity. Optimizing for the maximum kinetic energy will contribute to a finalization of material selection and parameters. The finalized rotor design will be used in the development of a dynamic model that is required for the control of the rotor. If it is discovered that a constraint is needed for the weight of the flywheel, this will be an easy addition to the optimization codes. The weight limit will depend on the levitation forces that can be produced with the magnetic Halbach array and superconductors.

5.2 Future Work

Further validation of model's accuracy is needed. The easiest way is to compare this model to that of an FEA model. Using the same material properties for each physical ring will allow for the comparison of the model with that of the isotropic equations. The stress is

shown to be similar to that of the plain stress model for an isotropic material. The discrepancy of the displacement will need to be compared to the FEA model. This may result in a need to adjust the displacement output of the model. The target speed for the low-speed UIFESS is 1,800 rpm. If the speed can safely be increased up to 4-5,000 rpm, there may be enough radial displacement for the position sensors to read. Balancing issues removes the possibility of placing strain gauges and data acquisition devices on the flywheel.

The iron laminations and stainless steel caps are the weakest components of the rotor itself. Further research is needed for possible solutions to resolve these issues. Complex geometry of the iron laminations need for the FRRM results stress concentrations. The ideal shape is a simple ring. Similar problems arise for the magnets and stainless steel caps. Stainless steel and the iron laminations have a density that is approximately four times great than the composite material that would be used. This increased density decreases the energy density and increases the stress in the rotor. If the density of the iron laminations is half of the actual value, the hoop stress in the laminations would decrease by approximately 100 MPa according to the model.

This large decrease in stress and density has steered focus to possible replacements. One possible solution is use of chopped fiber composites. To achieve the magnetic properties need to create a flux path, iron particles could be doped into the composite. An advantage for this, other than reducing weight, is the possibility of having iron deposits in locations needed for the FRRM such as that shown Figure 1.4. Where there is currently an airgap, a composite material with similar properties as the doped area can fill the void. This will result in the ideal ring shape therefore reducing the stress concentrations while

maintaining magnetic properties. Using iron particles decrease the effects of eddy current losses; however, it will reduce the amount of torque that can be induced.

Chopped fiber composites are typically used for cheaper, large quantity production. Applications of chopped fibers are focused towards lower stress applications due to low strengths. The strengths are largely dependent upon the shear strength of the lamina as shown in Equations 2.15 and 2.16. Bulk production for lower stress applications of chopped fibers has resulted in a lack of well-defined material properties. To determine if this method is feasible from the point of view of the FRRM, a permittivity test is required. This determines the volume fraction of the iron particles that would be needed. Mechanically, test specimens will need to be created and tested to determine strength, repeatability, and physical properties such the modulus. If the strength of this three material composite can come close to matching that of the iron laminations, it would be largely beneficial in decreasing stresses and increasing energy density. A reasonable strength chopped fiber composite could replace the stainless steel magnetic ring as well. This would allow for the magnets to be molded into the composite rather than pressed fitted which is currently the case.

The mass will likely be a limitation. If it is determined that the Halbach array will not support the optimized flywheel at 25,000 rpm then it will need to be added into the constraints for the optimization. Decreasing the outside radius, while maintaining the other dimensions, results in a drastic change in the stress at the outer portion and a marginal change at the iron laminations. If the stress is reduced enough, a more cost effective composite could be used in place of the carbon fiber. A stiff material is still needed to insure

ply separation does not occur. Stiff materials will also carry a greater load from the laminations but will also result in larger stress discontinuities.

Testing is required to validate the Poisson's ratios and shear modulus for the Hexcel carbon fiber composite as it is not currently given. Poisson's ratio can be a significant contributor to the overall displacement of the flywheel. With this, the overall flywheel, including the magnets, will require a full FEA analysis. This will insure geometries needed for the FRRM and the magnets won't experience failure. A finite element analysis will also determine if a ply will be needed that is oriented in a manner that is non-axisymmetric to increase strength and stiffness in the vertical direction.

5.3 Conclusion

The list below highlights the results of the work covered in this thesis.

- The development of a model to analyze the stress state of a multi-ring Flywheel Energy Storage System (FESS) is the primary objective for this thesis. A multi-ring flywheel incorporating fiber composites will be used for the design of the high-speed UIFESS. Fiber composites behavior is much different than that of isotropic materials. This consideration is included in the model. The increased strength in the hoop direction allows for higher rotational velocities. This model is and will be used to evaluate different materials for their use in the rotor design.
- Maintaining a one millimeter airgap is needed for control of the FRRM and the active magnetic bearing for stabilization. Adaptation of the model was done as a possible solution to maintain the airgap. High rotational speeds can induce large displacements which will reduce the forces that can be applied to the rotor from the stator. To maintain the required airgap the flywheel can be tapered such that when

expansion occurs, actuation of the plate will allow the gap to be maintained. This non-uniform shape will cause non-uniform expansion. The addition of angles between the iron-stainless steel and stainless steel-composite interface as shown in Figure 3.10 will reduce the extent of non-uniform displacement.

- A heuristic optimization method known as Particle Swarm Optimization (PSO) was formulated to interact with the model. The first optimization performed is one to minimize the change in displacement for the inner, tapered surface. The addition of slope between the interface surfaces can reduce the change in displacement. The optimum values depend on the taper of the inner surface. Results that the influence of the slope stainless steel-composite interface little effect on the displace values. At $\alpha = 5°$ and 50,000 rpm, the optimal values $\phi = 6.03°$ and $\beta = 2.65°$. Similar results were found at 20,000 rpm which concludes that interface slopes wouldn't be influenced by rotational velocity. The slopes are sensitive to the inner radius and the minimum thickness of iron laminations but less susceptible to influence from the outside radius of the carbon fiber. This is an effect of the large density of the iron laminations and the change in stress state as the inside radius is changed.
- Particle Swarm Optimization can also be tailored to maximize a value which is done by using Equation 4.5. The value that is of interest in this work is the kinetic energy. Bounds for the inner radius and ring thicknesses give many combinations flywheel designs. Many of these; however, would be incapable safely reaching high speeds. If no constraints are given, PSO would converge to a large, heavy, and fast set of design variables as a result of Equation 1.1. The limitation for yielding in the iron laminations based on the high hoop stress constrians the optimization function from

converging to that extreme location. This optimization gives a feasibility estimate for what is possible for the size and speed of the flywheel. The optimal size for the three ring design, with $\alpha = \phi = \beta = 0$ as defined in Figure 3.10 and radiuses defined in Figure 4.6, is $\mathbf{x}$ = [0.0394, 0.0544, 0.0608, 0.2631] meters at ω = 32,200 rpm. The stored kinetic energy 16 MJ with a mass of approximately 88 kg. Using the optimum size found at ω = 25,000 rpm, $\mathbf{x}$ = [0.0502, 0.0705, 0.0785, 0.2817] meters with a mass of 105 kg, has larger inner radius. This is preferred from an electrical aspect. Reducing the outside radius will result in a reduction of mass and energy but also stress. This is one way that a safety factor could be applied.

- Iron laminations are the weakest component of the flywheel even though they are closest to the axis of rotation. Substituting theses laminations with higher strength steel would allow for slightly higher velocities. Replacing the laminations with a material that is approximately half the density will result in reduction of the hoop stress by nearly 100 MPa. This would allow for larger velocity and therefore an increase in energy and energy density. Chopped fiber composite doped with iron particles is a possible solution. Much research and testing would be required to determine the feasibility of such a material. Equations used to approximate the strength of chopped fibers are discussed in Chapter 2. The derivation of those equations is done using well defined material properties. Chopped fibers are produced in bulk and have varying properties and have not been well tested. Strength testing is required for this composite. If the strengths shown by testing are comparable to the laminations, it would serve as an ample substitute.

References

[1] D. D. R. Williams, "Moon Fact Sheet," 25 February 2016. [Online]. Available: http://nssdc.gsfc.nasa.gov/planetary/factsheet/moonfact.html. [Accessed 18 March 2016].

[2] H. e. a. Chen, "Progress in electrical energy storage system: A critical review," *Progress in Natural Science,* vol. 3, no. 19, pp. 291-312, 2009.

[3] D. R. Brown and W. D. Chvala, "Flywheel energy storage: an alternative to batteries for UPS systems," *Energy Enineering,* vol. 5, no. 102, pp. 7-26, 2005.

[4] J. Scott et al, "NASA Technology Roadmaps TA 3: Space Power and Energy Storage," National Aeronautics and Space Administration, 2015.

[5] B. Bolund, H. Bernhoff and M. Leijon, "Flywheel energy and power storage systems," *Renewable & Sustainable Energy Reviews,* no. 11, pp. 235-238, 2007.

[6] I. Hadjipaschalis, A. Poullikkas and V. Efthimiou, "Overview of current and future energy storage technologies for electric power applications," *Renewable and Sustainable Energy Reviews,* no. 13, pp. 1513-1522, 2009.

[7] X. Lou, J. Wang, M. Dooner and J. Clarke, "Overview of current development in electrical energy storage technologies and the application potential in power system operation," *Applied Energy,* no. 137, pp. 511-536, 2014.

[8] B. Kisling, "Active Magnetic Bearing Control for an Experimental Flywheel Energy Storage System," Master's Thesis. University of Idaho, 2014.

[9] F. J. Wolff, "Flywheel Energy Storage Technology Being Developed," NASA Technical Reports Server, 2001.

[10] G. Sotelo, A. Ferreira and R. de Andrade, "Halbach Array Superconducting Magnetic Bearing for a Flywheel Energy Storage System," *IEEE TRANSACTIONS ON APPLIED SUPERCONDUCTIVITY,,* vol. 15, no. 2, pp. 2253-2256, 2005.

[11] S. S. Tinchev, "Enhanced superconductivity of YBCO interfaces: origin of high critical temperature in layered superconductors," *Nature,* pp. 1-13, Submitted 2009.

[12] J. D. Law, "Modeling of Field Regulated Reluctance Machines," University of Wisconsin-Madison, 1991.

[13] S. J. Chapman, Electric Machinery Fundamental, New York: McGraw-Hill, 2005.

[14] B. Wimer, "Dynamic Model and Design of an Integrated Flywheel Energy Storage," Master's Thesis. University of Idaho, 2014.

[15] K. Ramus, "Power Electronic Components and Hardware for an Experimental Flywheel Energy Storage System," Master's Thesis. University of Idaho, 2014.

[16] Y. Suzuki, A. Koyanagi, M. Kobayashi and R. Shimada, "Novel applications of the flywheel energy storage system," *Energy,* vol. 30, no. 11-12, pp. 2128-2143, 2005.

[17] L. Zhang, "The application of fiber materials in sports equipment," in *Education, Management, Information and Medicine,* Shenyang, 2015.

[18] A. Fink, D. B. Kolesnikov and H. Wilmes, "Hybrid Titanium Composite Material Improving Composite Structure Coupling," in *Materials for Aerospace Applications*, Paris, 2003.

[19] R. F. Gibson, Principles of Composite Material Mechanics, 3rd ed., Boca Raton: CRC Press, 2012.

[20] A. A. Griffith, "The Phenomena of Rupture an dFlow in Solids," *Philosophical Transactions of the Royal Society,* vol. 221A, pp. 163-198, 1920.

[21] R. Stephens, A. Fatemi, R. Stephens and H. Fuchs, Metal Fatigue in Engineering, 2nd ed., New York: Wiley-Interscience, 2001, p. 80.

[22] P. E. Chen, "Strength properties of discontinuous fiber composites: I. Fiber reinforced composites.," *Polymer Engineering and Science, 18(6),* pp. 496-504, 1971.

[23] J. K. Lees, "A study of the tensile stregnth of short fiber reinforced plastics.," *Polymer Engineering and Science, 8(3),* pp. 195-201, 1968.

[24] E. J. Hearn, Mechanics of materials 2: An Introduction to the Mechanics of Elastic and Plastic Deformation of Solids and Structural Materials, 3rd ed., Oxford: Butterworth-Heinemann, 1997, pp. 117-140.

[25] R. Jain, K. Ramachandra and K. Simha, "Rotating anisotropic disc of uniform strength," *International Journal of Mechanical Sciences,* vol. 41, no. 6, pp. 639-648, 1999.

[26] X.-L. Peng and X.-F. Li, "Effects of gradient on stress distribution in rotating functionally graded solid disks," *Journal of Mechanical Science and Technology,* vol. 26, no. 5, pp. 1483-1492, 2012.

[27] S. Ha and e. al, "Design, Fabrication and Testing of a Hybrid Composite Flywheel Rotor & Hub," in *International Conference on Composite Materials*, Jeju Island, Korea, 2011.

[28] M. Uddin, E. Morozov and K. Shankar, "Stress Analysis of a Filament Wound Composite Flywheel Disk," in *International Conference on Composite Materials*, Montreal, Canada, 2013.

[29] M. Tahani, A. Nosier and S. Zebarjad, "Deformation and stress analysis of circumferentially fiber-reinforced composite disks," *International Journal of Solids and Structures*, vol. 42, no. 9-10, pp. 2741-2754, 2005.

[30] S. K. Ha, H.-I. Yang and D.-J. Kim, "Optimal Design of a Hybrid Composite Flywheel with a Permanent Magnet Rotor," *Journal of Composite Materials*, vol. 33, no. 16, pp. 1544-1575, 1999.

[31] AKSteel, "Nonoriented Electrical Steels," July 2007. [Online]. Available: http://www.aksteel.com/pdf/markets_products/electrical/non_oriented_bulletin.pdf. [Accessed 15 February 2016].

[32] H. Corporation, "HexTow® HM63 carbon fiber," 12 October 2015. [Online]. Available: http://www.hexcel.com/Resources/Documents/HexTow_HM63_Flyer.pdf. [Accessed 28 March 2016].

[33] J. Arora, Introduction to Optimum Design, 3rd ed., Waltham, MA: Academic Press, 2012, pp. 51,135,142.

[34] J. Cheng and M. Druzdzel, "Latin Hypercube Sampling in Bayesian Networks," in *International Florida Artificial Intelligence Research Society Conference*, Orlando, 2000.

[35] R. Eberhart and J. Kennedy, "A New Optimizer Using Particle Swarm Theory," in *Micro Machine and Human Science*, Nagoya, 1995.

[36] R. Eberhart and Y. Shi, "Particle Swarm Optimization: Developments, Applications and Resources," in *Evolutionary Computation*, Seoul, 2001.